

RESEARCH ARTICLE

10.1002/2015JD023429

Key Points:

- Crucial V-V and V-T rates controlling CO₂ IR emission have been retrieved
- These rates are very different from current values and are much more accurate
- They are important for CO₂ measurements in the mesosphere and lower thermosphere

Correspondence to:

M. López-Puertas,
puertas@iaa.es

Citation:

Jurado-Navarro, Á. A., M. López-Puertas, B. Funke, M. García-Comas, A. Gardini, G. P. Stiller, and T. von Clarmann (2015), Vibrational-vibrational and vibrational-thermal energy transfers of CO₂ with N₂ from MIPAS high-resolution limb spectra, *J. Geophys. Res. Atmos.*, 120, 8002–8022, doi:10.1002/2015JD023429.

Received 26 MAR 2015

Accepted 6 JUL 2015

Accepted article online 14 JUL 2015

Published online 15 AUG 2015

Vibrational-vibrational and vibrational-thermal energy transfers of CO₂ with N₂ from MIPAS high-resolution limb spectra

Á. A. Jurado-Navarro¹, M. López-Puertas¹, B. Funke¹, M. García-Comas¹, A. Gardini¹, G. P. Stiller², and T. von Clarmann²

¹Instituto de Astrofísica de Andalucía, CSIC, Granada, Spain, ²Institute for Meteorology and Climate Research, Karlsruhe Institute of Technology, Karlsruhe, Germany

Abstract We present a retrieval of several vibrational-vibrational (V-V) and vibrational-thermal (V-T) collisional rate coefficients affecting the populations of the CO₂ levels emitting at 10, 4.3 and 2.7 μm from high-resolution limb atmospheric spectra taken by Michelson Interferometer for Passive Atmospheric Sounding (MIPAS). This instrument has a high spectral resolution (0.0625 cm⁻¹) and a wide spectral coverage (from 685 to 2410 cm⁻¹) that allow measuring and discriminating among the many bands originating the atmospheric 4.3 μm radiance. Also its high sensitivity allows measuring the atmospheric limb emission in a wide altitude range, from 20 to 170 km in its middle and upper atmosphere modes, and hence obtain information on the temperature dependence of the collisional rates. In particular, we retrieve the rate coefficients and their temperature dependence in the 130–250 K range of the following processes: CO₂(v_d, v₃) + N₂ ⇒ CO₂(v_d, v₃ - 1) + N₂(1) with v_d = 2v₁ + v₂ = 2, 3, and 4; CO₂(v₁, v₂, l, 1, r) + M ⇒ CO₂(v'₁, v'₂, l', 1, r') + M with Δv_d = v'_d - v_d = 0 and Δl = 0; and with Δv_d = 0 and Δl ≠ 0. In addition we have also retrieved the thermal relaxation of CO₂(v₃) into the v₁ and v₂ modes, e.g., CO₂(v_d, v₃) + M ⇒ CO₂(v'_d, v₃ - 1) + M with Δv_d = 2–4 and Δv₃ = -1 and the efficiency of the excitation of N₂(1) by O(¹D). All of them were retrieved with a much better accuracy than were known before. The new rates have very important effects on the atmospheric limb radiance in the 10, 4.3 and 2.7 μm spectral regions (5–8% at 4.3 μm) and allow a more accurate inversion of the CO₂ volume mixing ratio in the mesosphere and lower thermosphere from measurements taken in those spectral regions.

1. Introduction

Carbon dioxide, CO₂, is an important greenhouse gas playing an essential role in the energy budget of the atmosphere. In particular, it is responsible for the large radiative cooling of the upper mesosphere and lower thermosphere, and hence, it is one of the major drivers of the temperature of these atmospheric regions [López-Puertas and Taylor, 2001; Garcia et al., 2014]. CO₂ in the middle and upper atmosphere, where its mixing ratio starts to decrease with height, has been measured by different techniques, see López-Puertas et al. [2000] for a review. These include absorption measurements using the solar occultation technique, e.g., as taken by Atmospheric Trace MOlecule Spectroscopy aboard Spacelab 3 [Rinsland and Goldman, 1992] or the Atmospheric Chemistry Experiment (ACE) on the SCISAT-1 [Beagley et al., 2010]; as well as observations measuring the atmospheric limb emission in the near IR, mainly at 4.3 μm. The latter comprise several spaceborne instruments as the Stratospheric and Mesospheric Sounder (SAMS) on Nimbus 7 [Drummond et al., 1980; López-Puertas and Taylor, 1989], the Improved Stratospheric and Mesospheric Sounder (ISAMS) on Upper Atmospheric Research Satellite (UARS) [López-Puertas et al., 1998a, 1998b]; the CRyogenic Infrared Spectrometers and Telescopes for the Atmosphere (CRISTA) experiment on the space shuttle [Kaufmann et al., 2002], and more recently the Sounding of the Atmosphere using Broadband Emission Radiometry (SABER) on the NASA Thermosphere-Ionosphere-Mesosphere energetics and Dynamics (TIMED) [Mertens et al., 2009; Rezac et al., 2015], and the Michelson Interferometer for Passive Atmospheric Sounding (MIPAS) on Envisat [Fischer et al., 2008]. The analyses using the atmospheric emission spectra, however, require accurate and sophisticated modeling of the non-LTE populations of the states emitting at 10, 4.3, and 2.7 μm, which, being pumped by absorption of solar radiation, are largely controlled by collisional vibrational-vibrational and vibrational-thermal energy transfers to/from N₂.

These collisional processes were first used in the analysis of the atmospheric near-IR emission taken in the early days by several rockets experiments like Spectral Infrared Rocket Experiment (SPIRE), Spectroscopic Infrared Structure Signatures Investigation, or SPECTRAL InFRARED Interferometric Telescope (see López-Puertas and Taylor [2001] for a review). The rates of the vibrational-vibrational (V-V) and vibrational-thermal (V-T) processes are, however, poorly known. Only a few of them have been measured in the laboratory and when so, measurements were done long time ago as, e.g., the V-V transfer rate between $\text{CO}_2(00^0 1)$ and $\text{N}_2(1)$ [Inoue and Tsuchiya, 1975]. Sometimes they were also derived from atmospheric emission observations [Nebel et al., 1994] but with large uncertainties and assuming a reference background atmosphere because the atmospheric state was not measured simultaneously.

The MIPAS instrument on board Envisat has provided unprecedented measurements that allow us to advance our knowledge of these energy transfer processes. The main advantages of MIPAS are the following: (i) the high spectral resolution of the spectra (the unapodized spectral resolution of MIPAS data measured in the years 2005–2012 is 0.0625 cm^{-1}), which allows us to discriminate rovibrational lines from many different bands originating in the $4.3 \mu\text{m}$ region; (ii) its wide spectral range, measuring from $15 \mu\text{m}$ (used to derive the kinetic temperature) to the 10 and $4.3 \mu\text{m}$ regions (where many CO_2 energy levels at $4.3 \mu\text{m}$ and higher energies emit); (iii) the high sensitivity of the instrument (enabling to obtain high signal/noise spectra); and (iv) its global latitude coverage (measuring from pole to pole). MIPAS measured the $15\text{--}4.3 \mu\text{m}$ atmospheric limb emission in the altitude range from 20 to 170 km in the middle and upper atmosphere observation modes from 2005 until 8 April 2012 offering a large and invaluable data set.

The main aim of this work is to use MIPAS spectra to improve our knowledge of the collisional processes governing the non-LTE (local thermodynamic equilibrium) populations of the CO_2 levels emitting at 10, 4.3, and $2.7 \mu\text{m}$. In particular, we provide new information on the kinetic rates of the V-T deactivation of the $\text{CO}_2 v_3$ quanta in collision with N_2 and O_2 molecules; the V-V exchange rate of the $v_3 = 1$ quanta of $\text{CO}_2(v_1, v_2, l, v_3, r)$ (We follow here the HITRAN notation (v_1, v_2, l, v_3, r) for the CO_2 excited states, where v_j is the quantum number associated with the normal mode of vibration j , l is the vibrational angular momentum quantum number associated with the degenerate bending mode 2, and r is the ranking index, which is unity for the highest vibrational level of a Fermi resonating group [Rothman and Young, 1981; Rothman et al., 2005]. Table 2 shows the corresponding Herzberg notation. We also use the compressed notation (v_d, v_3) that represents all levels with $v_d = 2v_1 + v_2$, independently of the values of l and r .) levels with $\text{N}_2(1)$; and the collisional coupling between the $\text{CO}_2(v_1, v_2, l, v_3, r)$ and $\text{CO}_2(v'_1, v'_2, l', v_3, r')$ states in collisions with air molecules. A preliminary attempt to estimate some of these rates was reported by López-Puertas et al. [2005]. Here we present a detailed retrieval of these rates by using the method described by Funke et al. [2001] and with the concurrence of the Generic RADIative tranSfer ANd non-LTE population Algorithm (GRANADA), recently developed at Instituto de Astrofísica de Andalucía (IAA) [Funke et al., 2012], and the IMK (Institute for Meteorology and Climate Research)-IAA inversion processor [von Clarmann et al., 2003a], both of which uses the Karlsruhe Optimized and Precise Radiative transfer Algorithm (KOPRA) [Stiller et al., 2002]. In section 2 we describe the MIPAS observations; in sections 3 and 4 the retrieval method of the collisional rate coefficients and the non-LTE model are detailed. Section 5 describes the sensitivity of the MIPAS spectra to the collisional rates. The performance of the retrieval and the error estimations are discussed in section 6. For this purpose, synthetic spectra were inverted. In section 7 we present the retrieved collisional rates, their errors and their quality. In section 8 we discuss them on the light of previous measurements and values used in previous works. The major conclusions are summarized in section 9.

2. MIPAS Observations

The MIPAS instrument is a midinfrared limb emission spectrometer designed and operated for measurement of atmospheric trace species from space [Fischer et al., 2008]. It was part of the payload of Envisat launched on 1 March 2002 with a Sun-synchronous polar orbit of 98.55°N inclination and an altitude of 800 km. MIPAS had a global coverage from pole-to-pole passing the equator from north to south at 10:00 A.M. local time 14.3 times a day and taking daytime and nighttime profiles of spectra. The instrument's field-of-view is 30 km in horizontal and approximately 3 km in vertical direction. From January 2005 until the end of Envisat's operations on 8 April 2012, MIPAS measured at a reduced spectral resolution of 0.0625 cm^{-1} . Here we use MIPAS observations taken in the upper atmosphere (UA) mode with an along-tracking horizontal sampling of about 515 km recording a rear viewing sequence of 35 spectra every 63 s [De Laurentis, 2005; Oelhaf, 2008].

The UA mode covers the upper stratosphere, the mesosphere, and the lower thermosphere using 35 tangent heights from 172 km down to 42 km, with a sampling of 5 km from 172 to 102 km, and 3 km below. Here we use the daytime spectra taken during four days in 2010 (17 January, 30 March, 8 June, and 26 September), covering solstice and equinox conditions in both hemispheres. Version V5 (5.02/5.06) of the L1b-calibrated and L1b-geolocated spectra performed by the European Space Agency (ESA) were used here [Perron *et al.*, 2010; Raspollini *et al.*, 2010].

3. The Inversion Method

Collisional rate coefficients were retrieved jointly with the CO₂ profiles using the MIPAS level 2 (L2) processor developed and operated by IMK in Karlsruhe together with IAA in Granada. The processor is based on a constrained nonlinear least squares algorithm with Levenberg-Marquardt damping [von Clarmann *et al.*, 2003b]. Calculated spectra are fitted to the measured ones in an iterative way by updating the actual vector of retrieval variables \mathbf{x}_i of iteration i by

$$\mathbf{x}_{i+1} = \mathbf{x}_i + \left(\mathbf{K}_i^T \mathbf{S}_y^{-1} \mathbf{K}_i + \mathbf{R} + \lambda \mathbf{I} \right)^{-1} \times \left[\mathbf{K}_i^T \mathbf{S}_y^{-1} (\mathbf{y}_{\text{meas}} - \mathbf{y}(\mathbf{x}_i)) - \mathbf{R} (\mathbf{x}_i - \mathbf{x}_a) \right] \quad (1)$$

where \mathbf{y}_{meas} are the MIPAS measurements and \mathbf{S}_y is the measurement noise covariance matrix. \mathbf{K}_i is the Jacobian matrix containing the partial derivatives $\partial \mathbf{y}(\mathbf{x}_i) / \partial \mathbf{x}_i$, \mathbf{K}_i^T its transpose, and \mathbf{R} is a regularization matrix. The scalar times the identity matrix, $\lambda \mathbf{I}$, is the Levenberg-Marquardt damping term [Levenberg, 1944; Marquardt, 1963] which is forced to be zero in the last iteration. The term $\mathbf{y}(\mathbf{x}_i)$ is the result of the nonlinear radiative transfer model KOPRA, and the vector \mathbf{x}_a represents the a priori assumption of the unknown parameters.

In order to stabilize the retrieval, a priori assumptions are used. The collisional rates are constrained to related a priori assumptions using a diagonal regularization matrix containing the related a priori variances, in the sense of maximum a posteriori [Rodgers, 2000]. For the jointly fitted CO₂ profile, a Tikhonov-type smoothing constraint [Tikhonov, 1963] is used together with a strong diagonal constraint below 70 km. The latter forces the retrieved CO₂ in the stratosphere and lower mesosphere to be close to the well-known CO₂ mixing ratio in the homosphere. CO₂ a priori profiles have been taken from Whole Atmosphere Community Climate Model with specified dynamics (SD-WACCM) simulations [Garcia *et al.*, 2014] which is constrained with output from NASA's Modern-Era Retrospective Analysis [Rienecker *et al.*, 2011] below approximately 1 hPa. Garcia *et al.* [2014] showed SD-WACCM simulations for Prandtl numbers (Pr) of 4 (standard) and 2, corresponding to lower and higher eddy diffusion coefficients, respectively. Here we used the simulations for $Pr = 2$, which gives an overall better agreement with ACE CO and CO₂ and MIPAS CO [Garcia *et al.*, 2014].

The retrievals are performed using selected spectral regions (microwindows) in the 4.3 and 10 μm regions which vary with tangent altitude in order to optimize computation time and minimize systematic errors [von Clarmann and Echle, 1998]. In particular, error propagation due to horizontal inhomogeneities have been minimized by excluding opaque spectral lines which are insensitive to tangent point conditions.

In addition to the target retrieval variables, a height- and wave number-independent radiance offset and a continuum-like optical depth profile (below 60 km) are fitted jointly for each microwindow in order to compensate for offset calibration errors and spectrally smooth atmospheric contributions not reproduced by the radiative transfer forward model.

To obtain the L2 data from L1b spectra a sequence of preprocessing steps are required: (i) Correction of the spectral shift, followed by the retrieval of temperature, horizontal temperature gradients, and elevation pointing from the 15 μm spectral region [García-Comas *et al.*, 2014]; (ii) extension of the retrieved temperature profile with NRLMSIS-00 [Picone *et al.*, 2002] above 100 km; (iii) implicit determination of pressure by means of hydrostatic equilibrium (total density is obtained from pressure and temperature and using the ideal gas law); (iv) retrieval of O₃ vmr (volume mixing ratio) from the 10 μm spectral region [Gil-López *et al.*, 2005]; and (v) generation of atomic oxygen O(³P) and O(¹D) profiles below 100 km with a photochemical model [Funke *et al.*, 2012] constrained by the O₃ and pressure/temperature data obtained in the previous steps. Above 100 km, we took the O₂ and the atomic oxygen concentrations from the NRLMSIS-00 model and also use the same photochemical model for the calculation of O(¹D) from the O₂ photodissociation (O₃ is not required in this region).

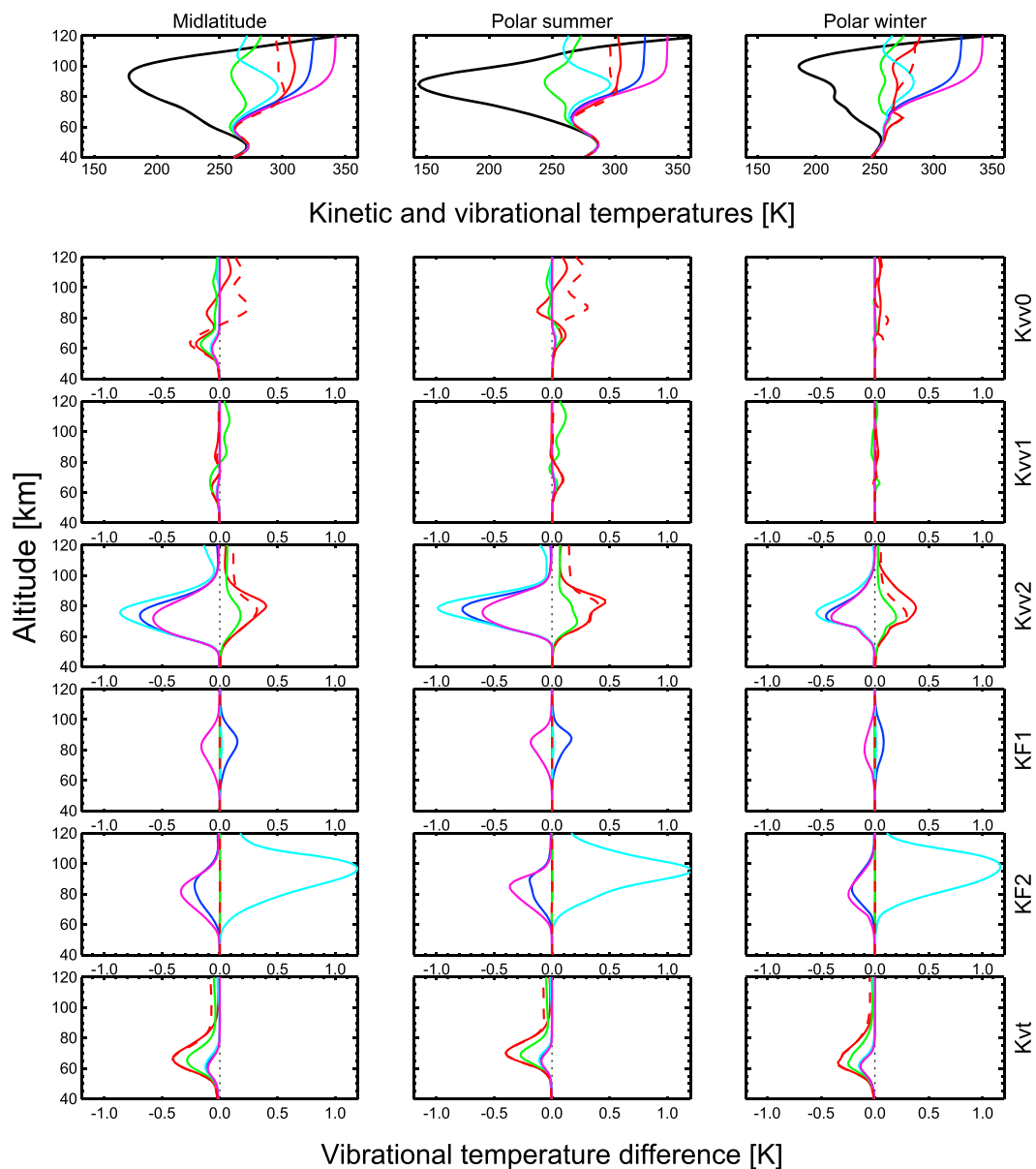


Figure 1. Change of the populations of the CO₂ 626 isotopologue levels 00011 (red solid), 01111 (green), 10012 (dark blue), 02211 (light blue), and 10011 (magenta), and of the 00011 level of isotopologue 636 (red dashed) for a 10% increase of the collisional rate coefficients for (left column) midlatitude, (middle column) polar summer, and (right column) polar winter conditions. (first row) Nominal vibrational temperatures and (second to seventh row) vibrational temperature changes due to an increase of k_{vv0} , k_{vv1} , k_{vv2} , k_{F1} , k_{F2} , and k_{vt} (see Table 1). The kinetic temperature profiles (black lines in the first row) and reference atmospheres were taken from the case of April at 45°N (SZA = 44.5°) for midaltitudes, from January at 75°S (SZA = 58.7°) for polar summer and from January at 75°N (SZA = 85.8°) for polar winter (see [Funke et al., 2012]).

4. Non-LTE Radiative Transfer Modeling

Vibrational populations of the six most abundant CO₂ isotopologues are calculated online during the retrieval with the GRANADA model. This generic non-LTE algorithm provides non-LTE populations for relevant atmospheric infrared emitters by solving iteratively the statistical equilibrium (SEE) and radiative transfer equations (RTE) under consideration of radiative, collisional, and chemical excitation processes. The current setup for CO₂ takes into account 134 vibrational levels, including ¹⁶O¹²C¹⁶O (isotopologue 1) levels up to (7,0), (6,1), (3,2), and (1,3) (here we follow the notation (v_d, v_3) with $v_d = 2v_1 + v_2$ referring to the Fermi groups, i.e., (2,0) including 10002, 01101, and 10001); ¹⁶O¹³C¹⁶O (isotopologue 2) levels up to (4,0), (4,1), and (0,2);

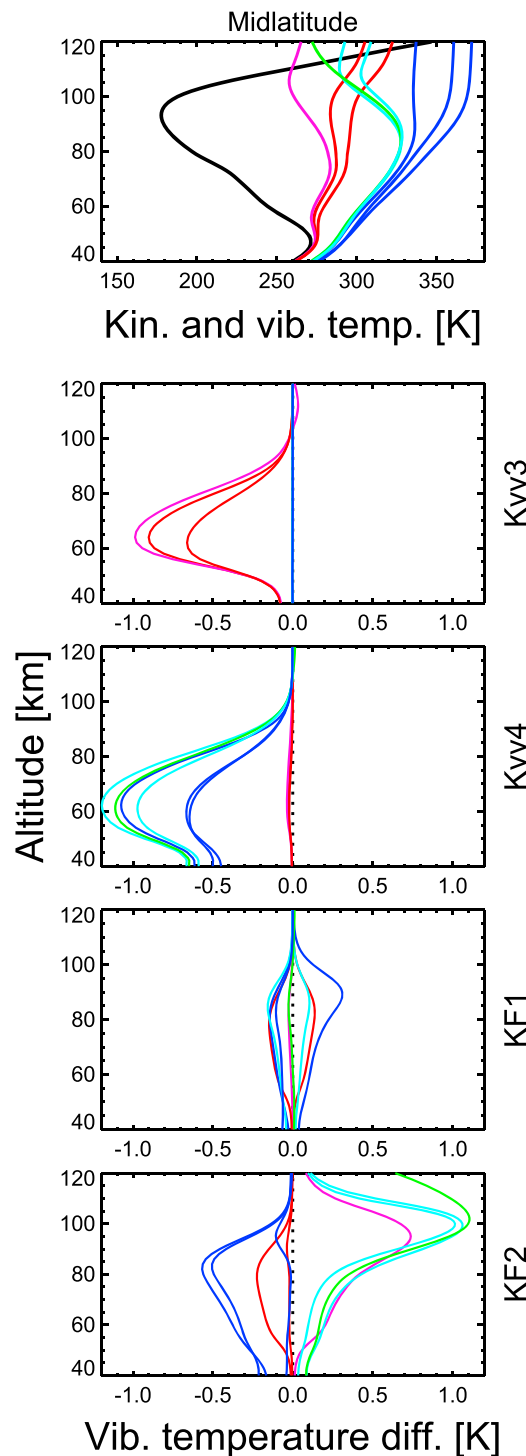


Figure 2. Changes of the populations of the CO₂ 626 isotopologue levels 03311 (magenta), 1111_r with $r = 1, 2$ (red), 04411 (green), 1221_r with $r = 1, 2, 3$ (light blue), and 2001_r with $r = 1, 2, 3$ (dark blue) for a 10% increase of the collisional rate constants for midlatitude conditions. (first panel) Nominal vibrational temperatures and (second to fifth panels) vibrational temperature changes due to an increase of k_{Vv3} , k_{Vv4} , k_{F1} , and k_{F2} . The kinetic temperature profile (black line in first panel) and reference atmospheres were taken from the case of April at 45°N (SZA = 44.5°) of Funke *et al.* [2012].

¹⁶O¹²C¹⁸O (isotopologue 3) and ¹⁶O¹²C¹⁷O (isotopologue 4) levels up to (3,0) and (2,1); and ¹⁶O¹³C¹⁸O and ¹⁶O¹³C¹⁷O (isotopologues 5 and 6) levels up to (1,0) and (0,1). The relative abundances of these isotopologues can be found in Table 6 of Rothman *et al.* [2005].

Because of the strong collisional coupling of CO₂ with N₂(1) via V-V energy transfer, vibrational populations of N₂(1) are also included in the non-LTE model. The SEE for N₂(1) is coupled into the SEE for the main CO₂ isotope. The CO₂ levels are connected by 695 radiative transitions, 39 of them considering full radiative transfer in the atmosphere. These 39 transitions involve vibrational states up to (4,1) for the main isotope; (3,0) and (2,1) for the 636 isotope; and (1,1) for the 628 and 627 isotopes. Above 20 km, radiative transfer is calculated using the modified Curtis matrix formalism [López-Puertas and Taylor, 2001]. The fundamental ν_2 band, as well as the ν_3 bands emitting at 4.3 μm and 2.7 μm (with $\nu_2 \leq 2$), are calculated line-by-line; for all other bands the equivalent line approach is used. The SEE for N₂(1) is coupled into the RTE calculation of the 00011→00001 band.

The calculated non-LTE populations are used for the forward calculation of the non-LTE radiative transfer and the determination of the Jacobian matrix performed by KOPRA. The non-LTE populations dependence on the target quantities correct the Jacobian matrix in the following manner

$$\mathbf{K} = (\partial \mathbf{y} / \partial \mathbf{x})|_{\mathbf{n}=\text{const}} + (\partial \mathbf{y} / \partial \mathbf{n}) \times (\partial \mathbf{n} / \partial \mathbf{x}), \quad (2)$$

where \mathbf{n} are the non-LTE populations, $\partial \mathbf{y} / \partial \mathbf{n}$ are the partial derivatives with respect to the non-LTE populations calculated by KOPRA, and $\partial \mathbf{n} / \partial \mathbf{x}$ are the derivatives of the non-LTE populations with respect to the target collisional parameters only, not to CO₂, provided also by the GRANADA model.

Variations of the local solar zenith angle (SZA) and temperature along the line of sight have a strong impact on the non-LTE populations and hence on 4.3 μm limb radiances, particularly in the summer hemisphere and for SZAs larger than $\sim 70^\circ$. They are therefore explicitly taken into account in the forward calculations using the method described by Funke *et al.* [2009].

Table 1. Energy Transfer Processes Studied in This Work^a

No.	Rate	Process	Rate Coefficient (cm ³ s ⁻¹) (Previous Works)	Rate (This Work) <i>k</i> ₀ ^c (or <i>f</i>)	<i>α</i> ^c
1	<i>k</i> _{vv0}	CO ₂ (<i>v</i> _{<i>d</i>} , <i>v</i> ₃) + N ₂ ⇒ CO ₂ (<i>v</i> _{<i>d</i>} , <i>v</i> ₃ - 1) + N ₂ (1); <i>v</i> _{<i>d</i>} = 0	5.0 · 10 ⁻¹³ √300/ <i>T</i>	4.64 ^d	0.64 ^d
2	<i>k</i> _{vv1}	CO ₂ (<i>v</i> _{<i>d</i>} , <i>v</i> ₃) + N ₂ ⇒ CO ₂ (<i>v</i> _{<i>d</i>} , <i>v</i> ₃ - 1) + N ₂ (1); <i>v</i> _{<i>d</i>} = 1	5.0 · 10 ⁻¹³ √300/ <i>T</i>	4.64 ^d	0.64 ^d
3	<i>k</i> _{vv2}	CO ₂ (<i>v</i> _{<i>d</i>} , <i>v</i> ₃) + N ₂ ⇒ CO ₂ (<i>v</i> _{<i>d</i>} , <i>v</i> ₃ - 1) + N ₂ (1); <i>v</i> _{<i>d</i>} = 2	5.0 · 10 ⁻¹³ √300/ <i>T</i>	5.02 ± 0.22	1.0
4	<i>k</i> _{vv3}	CO ₂ (<i>v</i> _{<i>d</i>} , <i>v</i> ₃) + N ₂ ⇒ CO ₂ (<i>v</i> _{<i>d</i>} , <i>v</i> ₃ - 1) + N ₂ (1); <i>v</i> _{<i>d</i>} = 3	5.0 · 10 ⁻¹³ √300/ <i>T</i>	5.61 ± 0.22	0.6
5	<i>k</i> _{vv4}	CO ₂ (<i>v</i> _{<i>d</i>} , <i>v</i> ₃) + N ₂ ⇒ CO ₂ (<i>v</i> _{<i>d</i>} , <i>v</i> ₃ - 1) + N ₂ (1); <i>v</i> _{<i>d</i>} = 4	5.0 · 10 ⁻¹³ √300/ <i>T</i>	5.64 ± 0.09	0.6
6	<i>k</i> _{F1}	CO ₂ (<i>v</i> ₁ , <i>v</i> ₂ ^l , 1) + M ⇒ CO ₂ (<i>v</i> ₁ ^l , <i>v</i> ₂ ^l , 1) + M; Δ <i>v</i> _{<i>d</i>} = 0, Δ <i>l</i> = 0 e.g., CO ₂ (10011) + M ⇒ CO ₂ (10012) + M	1.5 · 10 ⁻¹³ - 3 · 10 ⁻¹¹	7.04 ± 0.33	0.0
7	<i>k</i> _{F2}	CO ₂ (<i>v</i> ₁ , <i>v</i> ₂ ^l , 1) + M ⇒ CO ₂ (<i>v</i> ₁ ^l , <i>v</i> ₂ ^l , 1) + M; Δ <i>v</i> _{<i>d</i>} = 0, Δ <i>l</i> ≠ 0 e.g., CO ₂ (02211) + M ⇒ CO ₂ (10012) + M, or	1.5 · 10 ⁻¹³ - 2.4 · 10 ⁻¹²	5.57 ± 0.20	1.2
	<i>k</i> _{F2'}	CO ₂ (10011) + M ⇒ CO ₂ (02211) + M	3 · 10 ⁻¹³ - 4.8 · 10 ⁻¹²	5.57 ± 0.20	1.2
8a	<i>k</i> _{vt,a}	CO ₂ (<i>v</i> _{<i>d</i>} , <i>v</i> ₃) ^b + N ₂ ⇒ CO ₂ (<i>v</i> _{<i>d</i>} ^l , <i>v</i> ₃ - 1) + N ₂ ; Δ <i>v</i> _{<i>d</i>} = 2-4	<i>f</i> · (1.10 · 10 ⁻¹⁵ + 1.14 · 10 ⁻¹⁰ exp(-72.3/√ ³ <i>T</i>))(<i>f</i> = 1)	<i>f</i> = 0.82 ± 0.13	
8b	<i>k</i> _{vt,b}	CO ₂ (<i>v</i> _{<i>d</i>} , <i>v</i> ₃) + O ₂ ⇒ CO ₂ (<i>v</i> _{<i>d</i>} ^l , <i>v</i> ₃ - 1) + O ₂ ; Δ <i>v</i> _{<i>d</i>} = 2-4	<i>f</i> · (1.82 · 10 ⁻¹⁵ + 3.10 · 10 ⁻¹¹ exp(-63.3/√ ³ <i>T</i>))(<i>f</i> = 1)	<i>f</i> = 0.82 ± 0.13	
9	<i>k</i> _{O(1D)}	N ₂ + O(¹ D) → N ₂ (1) + O	<i>f</i> · ε · 2.1 · 10 ⁻¹¹ exp(115/ <i>T</i>); ε = 0.2 × 6.8 (<i>f</i> = 1)	<i>f</i> = 1.0 ± 0.15	
10	<i>k</i> _O	N ₂ (1) + O(³ P) → N ₂ + O	3.2 · 10 ⁻¹⁵ (<i>T</i> /300) ²⁻⁹	<i>f</i> = 2 ^d	

^aThe references of the rate coefficients used in previous works are given in section 8.

^b*v*_{*d*} = 2*v*₁ + *v*₂.

^c*k*₀ with estimated total errors (in units of 10⁻¹³ cm³s⁻¹) (see Table 3) and *α* as in *k* = *k*₀ (300/*T*)^{*α*}.

^dUsed (not retrieved) in this work.

5. Sensitivity of CO₂ Non-LTE Populations and 4.3 μm Limb Radiance to Collisional Rate Coefficients

In order to identify the collisional rate coefficients that have a detectable effect on the CO₂ vibrational populations and 4.3 μm limb radiances, we have carried out sensitivity studies for the most important rates that control their populations. Figures 1 and 2 show the vibrational temperature response of the main vibrational levels emitting at 4.3 μm (00011, 01111, 10011, 10012, and 02211 of the major isotopologue, and 00011 of the second one) to 10% changes of the collisional rates *k*_{vv,0}, *k*_{vv,1}, *k*_{vv,2}, *k*_{F1}, *k*_{F2}, and *k*_{vt} (see Table 1 and Figure 3). The responses of these populations to 10% changes in the *k*_{vv,3} and *k*_{vv,4} rates are very small and are not shown. As we expect the response to be dependent on the temperature distribution, the sensitivity has been performed for typical, i.e., midlatitudes, as well as extreme, polar summer- and polar winter-like, temperature profiles.

We see that there is a weak sensitivity to changes in *k*_{vv,0} and particularly in *k*_{vv,1} (lower than 0.2 K) but a significant response to changes of *k*_{vv,2}, *k*_{F1}, *k*_{F2}, and *k*_{vt}. The response to *k*_{vv,2} is particularly significant. The increase of this rate by 10% leads to a significant depletion of the populations of the 2.7 μm levels (10012, 02211, and 10011) and a simultaneous enhancement in the populations of the 00011 level of the two major isotopologues as well as that of 01111. Further, the response is found over a large-altitude region, covering 50 to 95 km. As expected, the response is smaller for polar winter conditions when the mesospheric temperature is larger and more isothermal. This large and altitude-extended response is very important since it would allow us to derive this rate accurately for different atmospheric conditions and therefore to gain information about its temperature dependence. The response to the changes of the rates in the CO₂ limb spectral radiance as would be measured by MIPAS are shown in Figures 4 and 5 for tangent heights of 60 and 80 km, respectively. The effect of perturbing *k*_{vv,0} and *k*_{vv,1} is very small, ≤0.2nW/(cm² sr cm⁻¹). This is about a factor of 15 smaller than the NESR (noise equivalent spectral radiance) of MIPAS in band D (1820–2410 cm⁻¹) of 3nW/(cm² sr cm⁻¹). Hence, the retrieval of these rates from single-MIPAS spectra (as we have performed for the other rates) would be very difficult and unstable. Therefore, we have not attempted to retrieve them. On the other hand, the spectra clearly show the decrease of the emission from the 4.3 μm second hot bands when perturbing *k*_{vv,2} for both tangent heights. These changes amount up to 3nW/(cm² sr cm⁻¹) at 60 km and 4.5nW/(cm² sr cm⁻¹) at 80 km. The effects of perturbing *k*_{vv,2} on the emission of the 4.3 μm fundamental

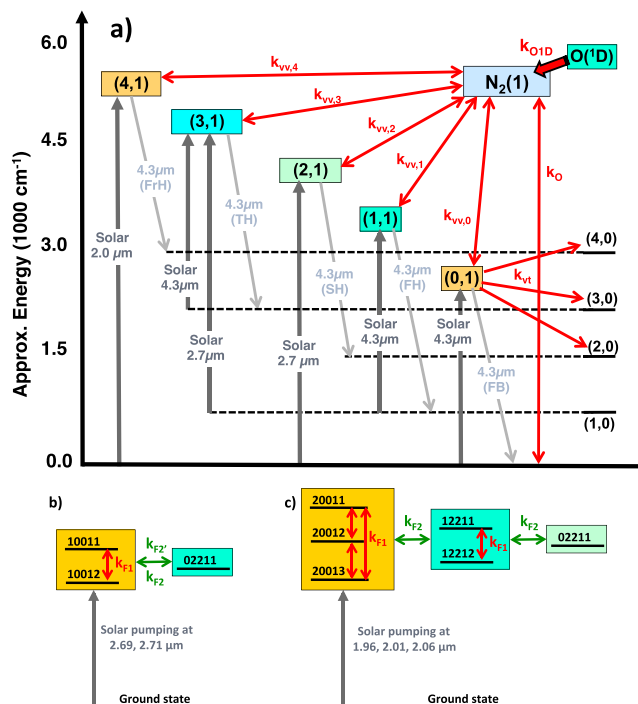


Figure 3. Schematic diagram showing the collisional rates considered in this work (see Table 1). (a) The processes $k_{vv,0}$, $k_{vv,1}$, $k_{vv,2}$, $k_{vv,3}$, $k_{vv,4}$, k_{vt} , and $k_{O(1D)}$ of the major CO_2 isotopologue (in red). The deactivation of $\text{N}_2(1)$ by $\text{O}(^3P)$, k_O , is also shown. The energy levels follow the (v_d, v_3) notation with $v_d = 2v_1 + v_2$. (b and c) The k_{F1} (in red) and k_{F2} (in green) processes for the $(v_d = 2, v_3 = 1)$ and $(v_d = 4, v_3 = 1)$ levels, respectively. k_{F2} and k_{F2} in Figure 3b correspond to the processes between (10011–02211) and (10012–02211), respectively. $\text{N}_2(1)$ and $\text{O}(^1D)$ energy levels are not at scale.

is much smaller ($\sim 0.5 \text{ nW}/(\text{cm}^2 \text{ sr cm}^{-1})$), and of opposite sign, but perceptible at a tangent height of 60 km (see Figure 4, fourth panel).

The effects of perturbing the rates affecting the redistribution of energy among the solar-pumped levels (k_{F1}) and between these and the adjacent nonpumped levels (k_{F2}) (see Table 1 and Figures 3b and 3c) are shown in Figure 1 (fifth and sixth rows) for the levels pumped by solar radiation in the 2.7 μm fundamental bands and in Figure 2 (fourth and fifth panels) for the higher levels pumped by solar radiation in the 2.7 μm first hot bands and in the 2.0 μm bands. As expected, k_{F1} perturbs only the solar-pumped levels, increasing the population of the more weakly pumped level, 10012, at the expense of the more excited 10011 state. Vibrational populations are affected by these processes between 60 km and 100 km. Similarly, increasing the rate of the collisional coupling of the solar pumped to the nonexcited levels depletes the populations of the former in favor of the latter. The enhancement of the nonpumped level is very large, extending to higher altitudes due to the absorption of upwelling radiation in the 4.3 μm hot band. We see similar effects in the higher-energy levels in Figure 2 (fourth and fifth panels). All of these levels emit in the 4.3 μm region, generating the second (SH), third (TH) and fourth (FrH) hot bands (see Table 2). The effects of the perturbations of these rates on the spectra as measured by MIPAS are shown in Figures 4 and 5 (eighth and ninth panels). We see that there is a significant change in the spectral radiance at both tangent altitudes, between about 1.5 and 3.5 $\text{nW}/(\text{cm}^2 \text{ sr cm}^{-1})$. The perturbations are more important at 80 km and k_{F2} shows a larger response.

The response of the population of the levels to the collisional rates $k_{vv,3}$ and $k_{vv,4}$ (see Table 1) are shown in Figure 2 (second and third panels). We see that only the more energetic levels directly affected by these rates are significantly perturbed while the populations of 00011, of the 2.7 μm levels, and of $\text{N}_2(1)$ (not shown) are hardly modified. That is important since the spectral lines of the bands originating from these levels will give us information on these rates, with no significant cross talk to other rate coefficients. It is also noticeable that the sensitivity region is lower than for other rates, with a peak at around 60 km and significant down to as far as 40 km. The levels directly affected by these rates generate the third and fourth hot bands near 4.3 μm (see Table 2). The mapping of the changes in their populations into the spectra are shown in Figures 4

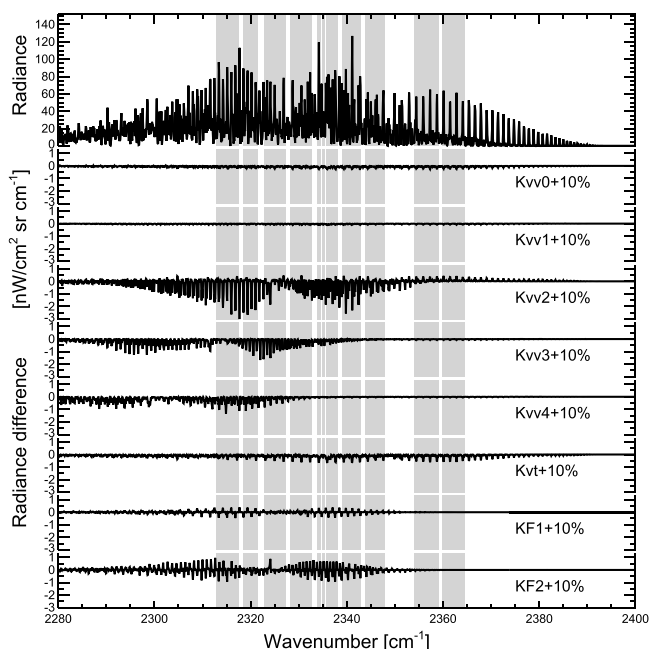


Figure 4. Sensitivity of CO₂ limb spectral radiances (tangent height of 60 km) as would be measured by MIPAS to a 10% increase of the collisional rate constants for midlatitude conditions (see Figures 1 and 2). (first panel) Simulated radiances and (second to ninth panels) radiance changes due to an increase of k_{VV0} , k_{VV1} , k_{VV2} , k_{VV3} , k_{VV4} , k_{Vt} , k_{F1} , and k_{F2} . Gray shaded regions indicate the spectral regions (microwindows) used in the retrieval of the rates.

and 5 (fifth and sixth panels) for 60 km and 80 km, respectively. They are significant, particularly at the 60km tangent height.

The sensitivity of the levels populations to k_{Vt} is shown in Figure 1 (seventh row). As expected, when the rate increases, the population of 00011 significantly decreases. All other energy levels hardly change, except 01111, which is also significantly depopulated. Although the region of the change of the population of 00011 to this rate is slightly overlapping with that of $k_{VV,2}$ (Figure 1, fourth row), they are very clearly distinguishable,

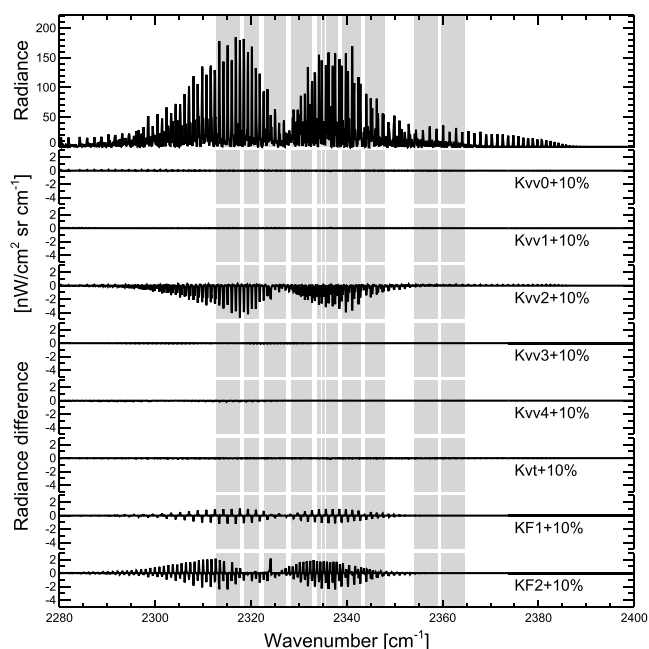


Figure 5. As in Figure 4 but for a tangent height of 80 km.

Table 2. Principal CO₂ Bands Emitting Near 4.3 μm Included in This Work

Iso ^a	Band	Upper Level ^b	Lower Level ^b	$\bar{\nu}_0$ (cm ⁻¹)	A ^d (s ⁻¹)
1	FB	(9) 00011 (00 ⁰ 1)	(1) 00001 (00 ⁰ 0)	2349.14	423.8
1	FH	(16) 01111 (01 ¹ 1)	(2) 01101 (01 ¹ 0)	2336.63	413.2
1	SH	(23) 10012 (02 ⁰ 1)	(3) 10002 (02 ⁰ 0)	2327.43	403.3
1	SH	(24) 02211 (02 ² 1)	(4) 02201 (02 ² 0)	2324.14	400.6
1	SH	(25) 10011 (10 ⁰ 1)	(5) 10001 (10 ⁰ 0)	2326.60	401.0
1	TH	(36) 11112 (03 ¹ 1)	(6) 11102 (03 ¹ 0)	2315.23	393.7
1	TH	(37) 03311 (03 ³ 1)	(7) 03301 (03 ³ 0)	2311.67	386.2
1	TH	(38) 11111 (11 ¹ 1)	(8) 11101 (11 ¹ 0)	2313.77	390.7
1	FHV ₃	(39) 00021 (00 ⁰ 2)	(9) 00011 (00 ⁰ 1)	2324.18	413.6
1	FrH	(43) 20013 (04 ⁰ 1)	(10) 20003 (04 ⁰ 0)	2305.26	385.0
1	FrH	(44) 12212 (04 ² 1)	(11) 12202 (04 ² 0)	2302.97	380.4
1	FrH	(47) 04411 (04 ⁴ 1)	(13) 04401 (04 ⁴ 0)	2299.21	370.2
1	FrH	(48) 20012 (12 ⁰ 1)	(12) 20002 (12 ⁰ 0)	2306.70	379.5
1	FrH	(49) 12211 (12 ² 1)	(14) 12201 (12 ² 0)	2301.06	378.4
1	FrH	(50) 20011 (20 ⁰ 1)	(15) 20001 (20 ⁰ 0)	2302.52	380.0
1	FHV ₃ ,FH	(51) 01121 (01 ¹ 2)	(16) 01111 (01 ¹ 1)	2311.70	806.5
1	5thH	(54) 21113 (05 ¹ 1)	(17) 21103 (05 ¹ 0)	2293.61	364.5
1	5thH	(56) 13312 (05 ³ 1)	(18) 13302 (05 ³ 0)	2290.68	368.4
1	5thH	(57) 05511 (05 ⁵ 1)	(20) 05501 (05 ⁵ 0)	2286.80	352.8
1	5thH	(58) 21112 (13 ¹ 1)	(19) 21102 (13 ¹ 0)	2293.41	370.7
1	5thH	(59) 13311 (13 ³ 1)	(21) 13301 (13 ³ 0)	2288.39	364.5
1	5thH	(60) 21111 (21 ¹ 1)	(22) 21101 (21 ¹ 0)	2289.90	369.5
1	FHV ₃ ,SH	(61) 10022 (02 ⁰ 2)	(23) 10012 (02 ⁰ 1)	2302.37	787.4
1	FHV ₃ ,SH	(62) 02221 (02 ² 2)	(24) 02211 (02 ² 1)	2299.24	781.8
1	FHV ₃ ,SH	(63) 10021 (10 ⁰ 2)	(25) 10011 (10 ⁰ 1)	2301.91	782.2
1	6thH	(64) 30014 (06 ⁰ 1)	(26) 30004 (06 ⁰ 0)	2283.30	367.9
1	6thH	(65) 22213 (06 ² 1)	(27) 22203 (06 ² 0)	2281.67	364.5
1	6thH	(66) 14412 (06 ⁴ 1)	(28) 14402 (06 ⁴ 0)	2278.39	353.2
1	6thH	(68) 30013 (14 ⁰ 1)	(29) 30003 (14 ⁰ 0)	2285.37	360.5
1	6thH	(69) 06611 (06 ⁶ 1)	(31) 06601 (06 ⁶ 0)	2274.42	333.4
1	6thH	(70) 22212 (14 ² 1)	(30) 22202 (14 ² 0)	2280.62	359.7
1	6thH	(71) 30012 (22 ⁰ 1)	(32) 30002 (22 ⁰ 0)	2283.58	358.7
1	6thH	(73) 14411 (14 ⁴ 1)	(33) 14401 (14 ⁴ 0)	2275.84	349.1
1	6thH	(74) 22211 (22 ² 1)	(34) 22201 (22 ² 0)	2277.17	357.4
1	6thH	(75) 30011 (30 ⁰ 1)	(35) 30001 (30 ⁰ 0)	2277.98	359.8
1	FHV ₃ ,TH	(76) 11122 (03 ¹ 2)	(36) 11112 (03 ¹ 1)	2290.25	768.4
1	FHV ₃ ,TH	(77) 03321 (03 ³ 2)	(37) 03311 (03 ³ 1)	2286.80	753.6
1	FHV ₃ ,TH	(78) 11121 (11 ¹ 2)	(38) 11111 (11 ¹ 1)	2289.08	762.0
1	SHV ₃	(79) 00031 (00 ⁰ 3)	(39) 00021 (00 ⁰ 2)	2299.26	1211.0
1	SHV ₃ ,FH	(93) 01131 (01 ¹ 3)	(51) 01121 (01 ¹ 2)	2286.80	1177.0
2	FB	(9) 00011 (00 ⁰ 1)	(1) 00001 (00 ⁰ 0)	2283.49	376.6
2	FH	(16) 01111 (01 ¹ 1)	(2) 01101 (01 ¹ 0)	2271.76	367.4
2	SH	(23) 10012 (02 ⁰ 1)	(3) 10002 (02 ⁰ 0)	2261.91	359.6
2	SH	(24) 02211 (02 ² 1)	(4) 02201 (02 ² 0)	2260.05	356.4
2	SH	(25) 10011 (10 ⁰ 1)	(5) 10001 (10 ⁰ 0)	2262.85	355.5
2	TH	(36) 11112 (03 ¹ 1)	(6) 11102 (03 ¹ 0)	2250.69	330.2
2	TH	(37) 03311 (03 ³ 1)	(7) 03301 (03 ³ 0)	2248.36	343.8

Table 2. (continued)

Iso ^a	Band	Upper Level ^b	Lower Level ^b	$\tilde{\nu}_0^c$ (cm ⁻¹)	A^d (s ⁻¹)
2	TH	(38) 11111 (11 ¹ 1)	(8) 11101 (11 ¹ 0)	2250.60	346.7
2	FHV ₃	(39) 00021 (00 ⁰ 2)	(9) 00011 (00 ⁰ 1)	2260.06	735.7
2	FrH	(43) 20013 (04 ⁰ 1)	(10) 20003 (04 ⁰ 0)	2240.54	344.1
2	FrH	(44) 12212 (04 ² 1)	(11) 12202 (04 ² 0)	2239.30	340.5
2	FrH	(47) 04411 (04 ⁴ 1)	(13) 04401 (04 ⁴ 0)	2236.68	329.8
2	FrH	(48) 20012 (12 ⁰ 1)	(12) 20002 (12 ⁰ 0)	2242.32	337.6
2	FrH	(49) 12211 (12 ² 1)	(14) 12201 (12 ² 0)	2238.57	336.1
2	FrH	(50) 20011 (20 ⁰ 1)	(15) 20001 (20 ⁰ 0)	2240.76	336.0
3	FB	(9) 00011 (00 ⁰ 1)	(1) 00001 (00 ⁰ 0)	2332.11	418.7
3	FH	(16) 01111 (01 ¹ 1)	(2) 01101 (01 ¹ 0)	2319.74	408.8
3	SH	(23) 10012 (02 ⁰ 1)	(3) 10002 (02 ⁰ 0)	2311.71	398.0
3	SH	(24) 02211 (02 ² 1)	(4) 02201 (02 ² 0)	2307.38	795.2
3	SH	(25) 10011 (10 ⁰ 1)	(5) 10001 (10 ⁰ 0)	2309.29	397.6
4	FB	(9) 00011 (00 ⁰ 1)	(1) 00001 (00 ⁰ 0)	2340.01	409.1
4	FH	(16) 01111 (01 ¹ 1)	(2) 01101 (01 ¹ 0)	2327.58	399.0
4	SH	(23) 10012 (02 ⁰ 1)	(3) 10002 (02 ⁰ 0)	2318.96	388.8
4	SH	(25) 10011 (10 ⁰ 1)	(5) 10001 (10 ⁰ 0)	2317.32	387.5
5	FB	(9) 00011 (00 ⁰ 1)	(1) 00001 (00 ⁰ 0)	2265.97	369.4
6	FB	(9) 00011 (00 ⁰ 1)	(1) 00001 (00 ⁰ 0)	2274.09	380.6

^aThe isotopologue numbers refer to those in the HITRAN compilation.

^bEnergy levels are given with the HITRAN identifier number (in parentheses) and the HITRAN and Herzberg (in parentheses) notations.

^cBand center.

^dEinstein coefficient at 250 K calculated from the HITRAN 2008 edition [Rothman *et al.*, 2009]. FB stands for fundamental band, FH for first hot ($\nu_d = 1$), SH for second hot ($\nu_d = 2$), TH for third hot ($\nu_d = 3$), FrH for fourth hot ($\nu_d = 4$), 5thH for fifth hot ($\nu_d = 5$), 6thH for sixth hot ($\nu_d = 6$), FHV₃ for ν_3 -first hot ($\nu_3 = 2$), FHV₃,FH for ν_3 -first hot ν_d -first hot ($\nu_3 = 2, \nu_d = 1$), FHV₃,SH for ν_3 -first hot ν_d -second hot ($\nu_3 = 2, \nu_d = 2$), FHV₃,TH for ν_3 -first hot ν_d -third hot ($\nu_3 = 2, \nu_d = 3$), SHV₃ for ν_3 -second hot ($\nu_3 = 3$), and SHV₃,FH for ν_3 -second hot ν_d -first hot ($\nu_3 = 3, \nu_d = 1$).

and hence, the emission from this energy level will provide independent information on the two parameters. The effects on simulated MIPAS spectra are shown in Figures 4 and 5 (seventh panel). We observe here that the major information comes from tangent heights closer to 60 km rather than 80 km.

In summary, we have demonstrated that MIPAS spectra in the altitude range from 40 to 100 km are very sensitive to the collisional rates $k_{VV,2}$, $k_{VV,3}$, $k_{VV,4}$, k_{F1} , k_{F2} , and k_{vt} (see Table 1). Furthermore, the different spectral responses and vertical structures of the perturbations of the rates provide independent information on each of the collisional parameters, and hence allows their joint retrieval and to gain information on their temperature dependencies. In the next section we further verify these results by applying the retrieval scheme to synthetic spectra.

6. Retrievals From Synthetic Spectra and Error Estimations

In this section we present the results of the joint inversion of the collisional rate coefficients and CO₂ vmr from synthetic spectra. The aim is to verify that the inversion scheme works as expected, to quantify how much information can be gained on each of the collisional rates, and to use this method to evaluate some systematic errors.

Synthetic spectra according to the MIPAS spectral specifications, including artificial NESR of 3nW/(cm² sr cm⁻¹), have been computed for the midlatitude, April 45°N reference atmosphere, SZA=44.5° [Funke *et al.*, 2012] using the non-LTE populations shown in Figures 1 and 2. Examples are shown in Figures 4 and 5 (first panel). We have performed retrievals of the state vector composed of the collisional rates $k_{VV,2}$, $k_{VV,3}$, $k_{VV,4}$, k_{F1} , k_{F2} , and k_{vt} , as well as the CO₂ abundance. The microwindows used in the joint retrieval are shown by the gray shaded regions in Figures 4 and 5 (note that they change with the tangent height) and they cover

emissions from all the 4.3 μm bands sensitive to these parameters (see Table 2). Additional microwindows in the 10 μm region in the lines arising from the 00011 \rightarrow 10002 band have also been included (not shown).

In the inversion of MIPAS spectra we have also derived the temperature dependencies of these rates, i.e., we have retrieved α in $k = k_0 (300/T)^\alpha$. This has been carried out in an iterative way by varying the parameter α and minimizing the χ^2 of the residuals. In these simulations, however, we assumed that this dependence, i.e., α , was known.

The joint retrieval of the collisional rates and CO_2 was performed with initial guess rates equal to the true values perturbed by 20%. The CO_2 profile was systematically perturbed by a 5% increase at 60–90 km and by a 20% increase above 90 km.

The results showed that all inverted parameters were retrieved within $\pm 1\%$ of their true values, and thus that the retrieval was not overregularized by the applied constraint. The CO_2 profile was also retrieved simultaneously with maximum deviations from the true profile smaller than 1% below 95 km, 1% at 100 km, and 3% at 110 km. Given the moderate vertical resolution of the retrieved CO_2 vmr profile (~ 4 km), we have also estimated the impact of a systematic bias in the a priori CO_2 profile, particularly around the homopause, where CO_2 abruptly decreases with altitude (see Figure 7). This has been done by performing the retrieval with a different a priori CO_2 profile taken from SD-WACCM simulations for Prandtl numbers of $Pr=4$ (instead of $Pr=2$ used in the standard case). *García et al.* [2014] have shown that the change in this parameter, equivalent to change the eddy diffusion parameter, significantly changes the altitude of the decrease of CO_2 . The impact on the retrieved rates is negligibly small with deviations from the true values smaller than 0.1%. Hence, these results demonstrate the ability of the retrieval scheme to simultaneously retrieve those rates and the CO_2 profile with a high precision and a reasonably weak dependence on the a priori assumptions.

We have used this method to perform sensitivity studies in order to estimate some of the known parameter errors in the retrieval of these parameters. Among those, we know that the abundances of atomic oxygen, $\text{O}(^3P)$, and $\text{O}(^1D)$, not measured simultaneously with MIPAS spectra, significantly affect to the population of the CO_2 levels [*López-Puertas and Taylor*, 2001; *Kaufmann et al.*, 2002]. The emission at 4.3 μm also depends very much on the solar flux, mainly at 4.3 and 2.7 μm .

$\text{O}(^3P)$ and $\text{O}(^1D)$ abundances, below about 95 km, are photochemically constrained by the retrieved O_3 from the same MIPAS spectra. Above 95 km, however, simultaneous O_3 observations are not available. $\text{O}(^3P)$ has a large variability and it is not well known in the mesosphere and lower thermosphere [*Kaufmann et al.*, 2014]. Following previous studies [*García-Comas et al.*, 2012, 2014] we have considered a 50% uncertainty in the $\text{O}(^3P)$ concentration. $\text{O}(^1D)$ has different major sources in the stratosphere/lower mesosphere and in the upper mesosphere/lower thermosphere. In the lower region it is mainly produced by O_3 photodissociation in the Hartley band (200–310 nm) [*Brasseur and Solomon*, 2005]. Since the uncertainty in the solar flux in this spectral region is not very large, the $\text{O}(^1D)$ uncertainty is dominated by the O_3 retrieval accuracy, estimated to be within 10% below 80 km. In the upper mesosphere/lower thermosphere $\text{O}(^1D)$ is mainly produced from the photodissociation of O_2 in the Lyman α and Schumann-Runge bands and continuum. The solar radiance at these wavelengths is rather uncertain [*Ermolli et al.*, 2013] and the computation of the photoabsorption coefficient requires high spectral resolution. Overall, we have considered an uncertainty of 30% in the abundance of $\text{O}(^1D)$ above 80 km.

Solar fluxes near 4.3, 2.7, and 2.0 μm are calculated in the GRANADA model considering the time-dependent Sun-Earth distance. Attenuation by solar Fraunhofer lines is taken into account [*Hase et al.*, 2006]. The solar background radiance is expressed as a blackbody with an effective temperature $T_e = 5450 + 0.25 \cdot (\tilde{\nu} - 2000)$, being $\tilde{\nu}$ wave number in cm^{-1} . This parameterization is similar to that developed by *Platnick and Fontenla* [2008] for 3.7 μm , and they agree within 0.5–1% at that wavelength. On the other hand, the calculated solar flux agrees within 0.1% with that of *Kurucz* [1995] in the 4.3, 2.7, and 2.0 μm spectral regions. Based on these results, we have assumed an error of 1% in the solar fluxes. The mapping of these errors on the retrieved collisional rates is listed in Table 3. This table also includes other sources of errors as the gain calibration uncertainty of MIPAS, and the systematic error of temperature. The first was estimated to be in 1% in band D [*Kaufmann et al.*, 2006, <http://www.atm.ox.ac.uk/group/mipas/err/>]. However, more recent estimates suggest that this error is slightly larger, i.e., 1.25% (G. Perron, private communication, 2015). The temperature errors were taken as 1 K from 50 to 70 km, 2 K between 70 and 80 km and 5 K above [*García-Comas et al.*, 2014].

Table 3. Errors of the Rate Coefficients Retrieved in This Work (See Table 1)

Rate	Errors (%)							Total
	Random	Gain(1.25%)	Temperature ^a	Tangent Altitude	[O(³ P)](50%)	[O(¹ D)] ^b	Solar Flux(1%)	
k_{VV2}	0.16	4.0	0.6	0.81	0.05	1.4	2.6	5.1
k_{VV3}	0.09	1.9	3.5	0.30	0.06	0.8	0.18	4.1
k_{VV4}	0.08	1.8	0.6	0.08	0.38	0.07	2.7	3.3
k_{F1}	0.09	0.8	4.6	1.2	0.22	0.11	0.33	4.8
k_{F2}	0.09	1.5	3.1	2.2	0.11	0.23	0.61	4.1
f_{vt}	0.19	9.2	2.9	0.47	3.1	11	4.3	15

^a 1 K at 50–70 km, 2 K at 70–80 km, and 5 K above 80 km.

^b 10% below 80 km and 30% above.

We also included the error introduced by the uncertainty in the elevation pointing (tangent altitude). This is retrieved jointly with temperature from the 15 μm spectral region [García-Comas *et al.*, 2014]. However, there is little information on it above ~ 60 km. von Clarmann *et al.* [2003b] estimated the total systematic error in the retrieved absolute pointing from 15 μm to be less than 200 m. Kiefer *et al.* [2007] characterized the accuracy of the engineering information of the MIPAS elevation pointing and found that the relative pointing errors, i.e., uncertainties in the altitude differences between adjacent tangent altitudes, are on average about 200 m. Hence, in order to estimate the total systematic pointing error, both components (absolute and relative) have to be taken into account. Combining them quadratically leads to an uncertainty of 283 m, that constitute the pointing error included in the retrieved rates (see Table 3). Given the high spectral resolution of MIPAS, propagated errors arising from interfering species in this spectral region are negligible.

Table 3 shows that the major uncertainties in the $k_{VV,2}$ rate originate from the gain and solar flux uncertainties, with a nonnegligible contribution from O(¹D). Adding all the sources quadratically they amount to a total error of 5.1%. The rate $k_{VV,4r}$, affecting also solar-pumped levels, has similar error sources but the uncertainties induced by the gain and O(¹D) are smaller. The uncertainty of the $k_{VV,3}$ rate coefficient, affecting to the deactivation of levels not directly excited by solar radiation, is mainly driven by the temperature error. The same occurs to the k_{F1} and k_{F2} rate coefficients with overall errors of 4.8% and 4.1%, respectively. The error in the vibrational-thermal k_{vt} rate is, however, larger. Several sources contribute significantly: the gain, the kinetic temperature, atomic oxygen, the solar flux and, principally, the uncertainty in the concentration of O(¹D).

7. Results

The results of the retrieved collisional rates for all of the daytime scans of the four days of MIPAS UA measurements are shown in Figure 6 as a function of latitude. The mean values are listed in Table 1. As discussed above we have retrieved the rates as well as its temperature dependence in the form of $k = k_0 (300/T)^\alpha$ through an iterative process. The mesospheric temperature changes significantly with latitude and season. However, Figure 6 shows that the retrieved k_0 values are essentially independent of latitude. This demonstrates that the retrieved temperature dependence, in the range of mesospheric temperatures, is very accurate. We estimated the error of α following the same procedure as we did for its derivation. We found that a perturbation of 10% introduces an appreciable increase in the χ^2 ; so this can be considered as an upper limit of its error.

In Table 1 we also list the factor retrieved for the rate $k_{O(1D)}$. This process enhances the population of N₂(1) and because of its strong $k_{VV,0}$ coupling with CO₂ also largely controls the population of 00011 in the mesosphere. This process has, however, the opposite effect of the thermal relaxation of 00011 by air molecules, k_{vt} (process 8 in Table 1), and hence could not be jointly retrieved with k_{vt} in the inversion. We then followed a similar strategy as for determining the rate temperature dependence. That is, we retrieve k_{vt} assuming different values for $k_{O(1D)}$. The retrievals showed that for small changes (<50%) around the a priori values of the rates, we obtained a near one-to-one response. We then assumed as the best retrieved (k_{vt} , $k_{O(1D)}$) pair the one that minimizes the χ^2 of the retrieval.

The retrieval noise, i.e., the mapping of the MIPAS NESR of 3 nW/(cm² sr cm⁻¹) into the rates, is generally very small (see gray shaded areas in Figure 6). However, the dispersion of the retrieved values is much larger than the noise error for all the rates. This suggests that the dispersion is caused by the random variability

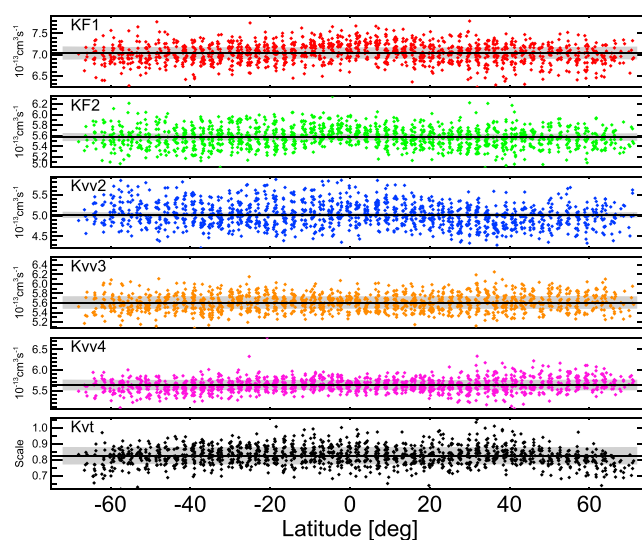


Figure 6. Retrieved collisional rates at 300 K, k_0 , as function of scan latitude for all of the daytime scans of MIPAS spectra taken in the UA mode during 17 January, 30 March, 8 June, and 26 September of 2010. The mean value from all latitudes is represented by solid lines. The gray shaded areas represent the noise error in the individual retrieved rates.

(stochastic errors) of the atmospheric parameters. Hence, we have estimated the random error of the retrieved collisional rates (see Table 3), including the propagated uncertainties of not accurately known parameters, as the standard error of the retrieved values derived from all scans (see Figure 6).

As mentioned above, we have retrieved the CO_2 vmr jointly with the collisional rates. Although we have found (see section 6) that there is only little dependence of the retrieved collisional rates on the CO_2 a priori profile, one may ask if the retrieved CO_2 is plausible, or if it is unrealistically biased. The latter could hint at a not yet identified systematic error source. Figure 7 shows the retrieved CO_2 profiles compared with colocated ACE measurements. There are very few contemporary measurements of CO_2 in the middle and upper atmosphere, only from ACE [Beagley *et al.*, 2010] and SABER [Mertens *et al.*, 2009; Rezac *et al.*, 2015]. SABER uses also the limb emission technique while ACE, using the solar occultation approach, is not affected by non-LTE. Hence, ACE observations were taken here for comparison. The CO_2 from SD-WACCM simulations ($Pr = 2$), which is used as a priori in the retrieval, is also shown for comparison. Due to the absorption technique used by ACE, there are very few profiles available for comparison (and located essentially only at two different latitudes). In order to get a meaningful statistic we then considered the ACE measurements taken with ± 3 days of the MIPAS measurements. We see that overall there is a very good agreement between the CO_2 of ACE and MIPAS. During solstice conditions (Figure 7, top row), the agreement is not as good but still within the error bars below ~ 100 km. Only during polar summer at altitudes above ~ 100 km, ACE and MIPAS profiles diverge, with MIPAS lying between the profile predicted by SD-WACCM and that measured by ACE. At northern latitudes the agreement is better. For equinox conditions, when the temperature and CO_2 gradients in the upper mesosphere/lower thermosphere are generally less pronounced, the agreement between ACE and MIPAS is excellent. In conclusion, the comparison of the jointly retrieved CO_2 vmr profiles to independent observations provides no hint at a systematic bias of the retrieved rates.

For a further check of the quality of the retrievals we looked at the spectral residuals at several tangent heights (see Figure 8). The residuals still show some systematic differences at lower tangent heights (73 km), but they are very small, in the order of $\pm 1 - 2$ nW/(cm^2 sr cm^{-1}), which is only $\sim 1\%$ of the signal. At smaller wave numbers (2280–2320 cm^{-1}), a large fraction of these differences can be attributed to the 4.3 μm fundamental band of second isotopologue, whose collisional rate with $\text{N}_2(1)$ was not retrieved here. This suggests that it is slightly different from the value for the most abundant isotopologue. Since rovibrational lines of the second isotopologue's fundamental band have been excluded from the microwindow selection, no impact on the retrieved rates is expected. At 82 km the signal is very similar to that at 73 km but the root-mean-square (RMS) has decreased by a factor of 1.3, leading to an even better simulation of the measurements. The major reason is the better simulation of the mentioned isotopic band. At 91 km, the residuals are smaller, even in relative terms. We still appreciate some systematic residuals coming mainly from the second hot bands. However,

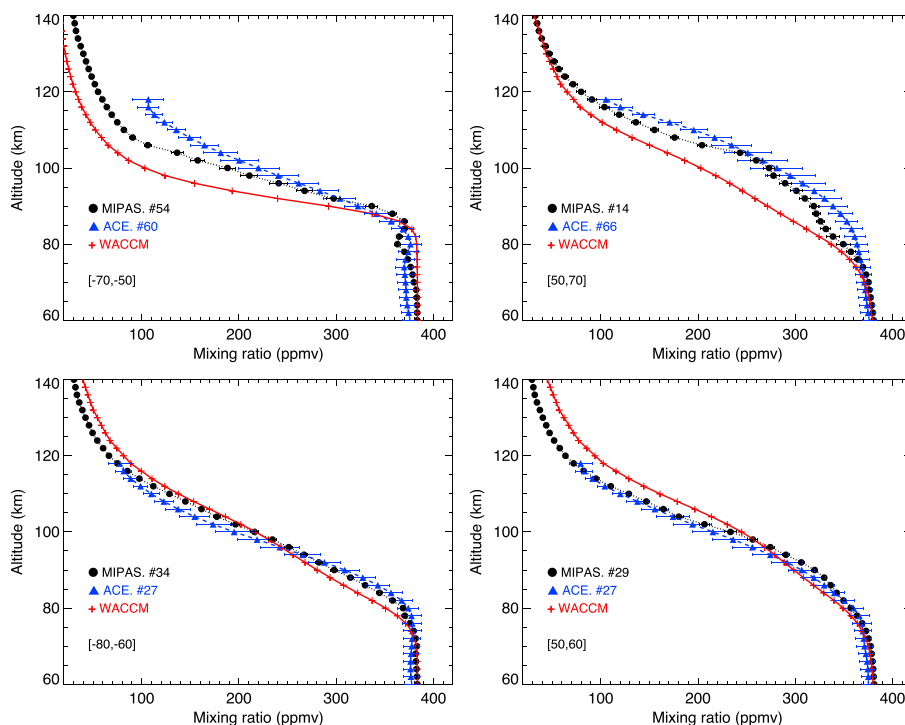


Figure 7. CO₂ vmrs retrieved jointly with the collisional rates and compared with colocated ACE measurements and the a priori SD-WACCM ($Pr = 2$) CO₂ profiles. (top row) Solstice conditions (17 January 2010) for (left column) southern (polar summer) and (right column) northern (polar winter) conditions and (bottom) equinox conditions (30 March 2010) (left and right columns, respectively). The error bars in the ACE profiles are the total (random and systematic errors) [Beagley *et al.*, 2010; Garcia *et al.*, 2014]. The small error bars of MIPAS represent only the noise error. Numbers in brackets give the latitude band, and those after “ACE” and “MIPAS” give the numbers of averaged profiles.

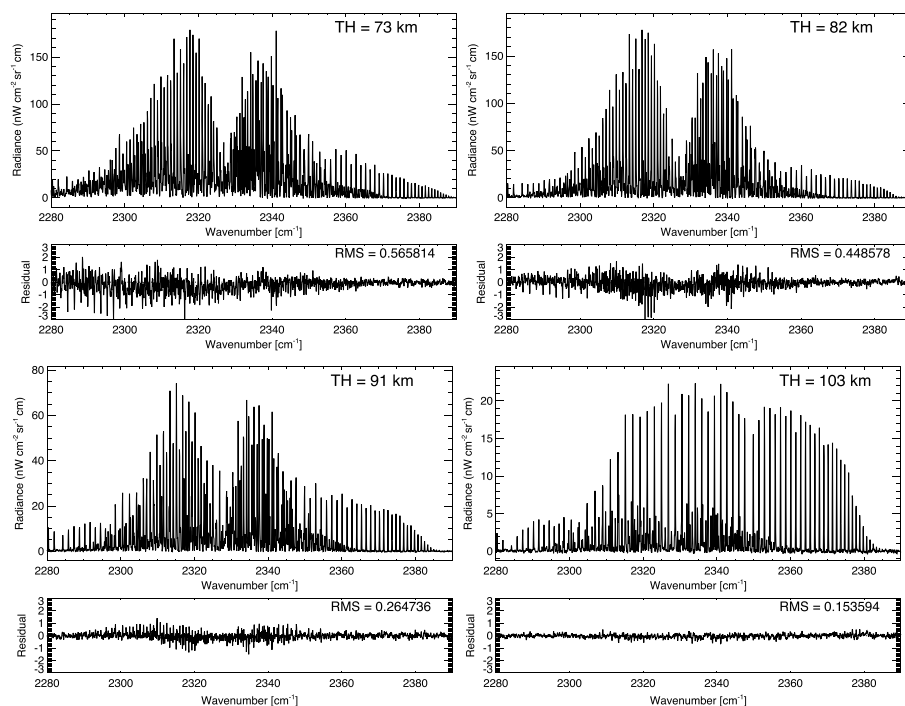


Figure 8. Coadded measured spectra and residuals, simulated – measured, at tangent heights of 73, 82, 91, and 103 km obtained from the retrievals for the four analyzed days. The residuals are in the same radiance units of $nW/(cm^2 sr cm^{-1})$.

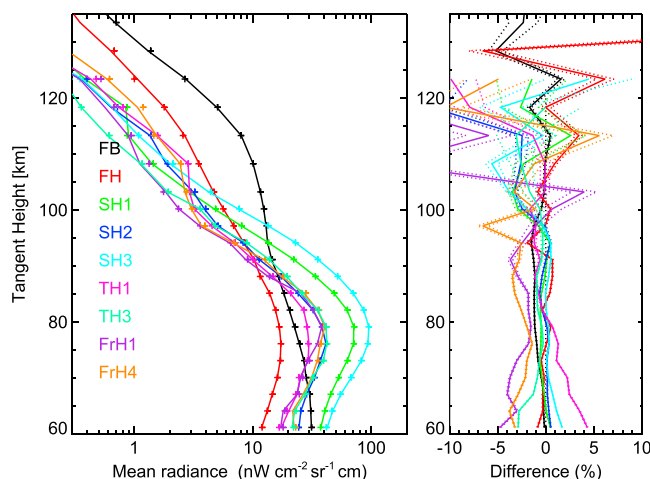


Figure 9. (left) Measured (symbols) and simulated (lines) mean radiances in the 2280–2400 cm^{-1} interval of different CO_2 4.3 μm bands (see Table 2) obtained in the retrievals for the four analyzed days (see Figure 8). (right) The differences (simulated-measured) in percentage and their standard deviations (dotted lines).

given the excellent agreement of the observed and modeled band-averaged radiances (see below), these residuals are most likely introduced by a systematic error in the kinetic temperature distorting the rotational distribution. At higher altitudes, we observe that the measured spectra are very well reproduced. Overall, we have not found any significant feature (i.e., larger than $\approx 1-2\%$ of the signal) in the residuals, which provides confidence on the retrieved collisional rates.

To show more clearly the residuals in the different CO_2 4.3 μm bands (see Table 2), we calculated the band-averaged radiance contributions in the measured and simulated spectra (see Figure 9). These were computed by weighting the total spectra by the line intensities of the corresponding band and normalizing it. Hence, they do not strictly represent the band contributions, since overlap and nonlinearity in the radiative transfer are not properly taken into account, but are a good estimate of their contributions. Thus, some bands with strong overlap, as FrH2 and FrH3 (see Table 2), were not shown. The very good agreement between measurements and simulations in all the bands and at all tangent heights is remarkable. The deviations are generally within $\pm 2-3\%$ and only at the uppermost tangent heights (above 115 km), where the signal to noise is smaller, the percentage deviations are slightly larger.

8. Discussion

In this section we discuss the retrieved collisional rates in the light of the values used in previous works and their effects on the CO_2 4.3 μm atmospheric emission. The rate $k_{vv,0}$ has not been retrieved here but it is discussed for completeness. This rate was measured by *Inoue and Tsuchiya* [1975] in the 150–300 K temperature range and it has been used as $k_{vv,0} = 5 \cdot 10^{-13} \sqrt{300/T}$ (see Table 1 and Figure 10a) in practically all the studies of the CO_2 atmospheric emission at 4.3 μm carried out so far. Thus, it was used in the analysis of SAMS measurements [López-Puertas and Taylor, 1989], of SPIRE observations [Nebel et al., 1994], and also introduced in the model of *Shved et al.* [1998] that was used in the retrieval of CO_2 from CRISTA spectra [Kaufmann et al., 2002] and more recently from SABER measurements [Rezac et al., 2015]. By the way, we noted a typographical error in process 7 of *Shved et al.* [1998], where it should be $1/\sqrt{T}$ instead of \sqrt{T} . The same rate was used by *Funke et al.* [2012]. Only the analysis of ISAMS measurements [López-Puertas et al., 1998a, 1998b] suggested that a factor between 0.8 and 1.0 times the rate of *Inoue and Tsuchiya* [1975] was consistent with ISAMS radiances taken at a SZA lower and higher than 60° , respectively. In our analysis we use the fit $k_{vv,0} = 4.64 \cdot 10^{-13} (300/T)^{0.64}$ to the measurements of *Inoue and Tsuchiya* [1975], which is very similar to the usual form of $k_{vv,0} = 5 \cdot 10^{-13} \sqrt{300/T}$ (see Figure 10a).

The rate coefficient $k_{vv,1}$, where the excited state of CO_2 is 01111, has been taken equal to the rate $k_{vv,0}$ of the V-V exchange between $\text{CO}_2(00011)$ and N_2 in all the studies mentioned above. Our simulations show that there is little sensitivity to this parameter (see Figure 1, third row) and hence has not been retrieved here. We have also assumed the same value as for $k_{vv,0}$.

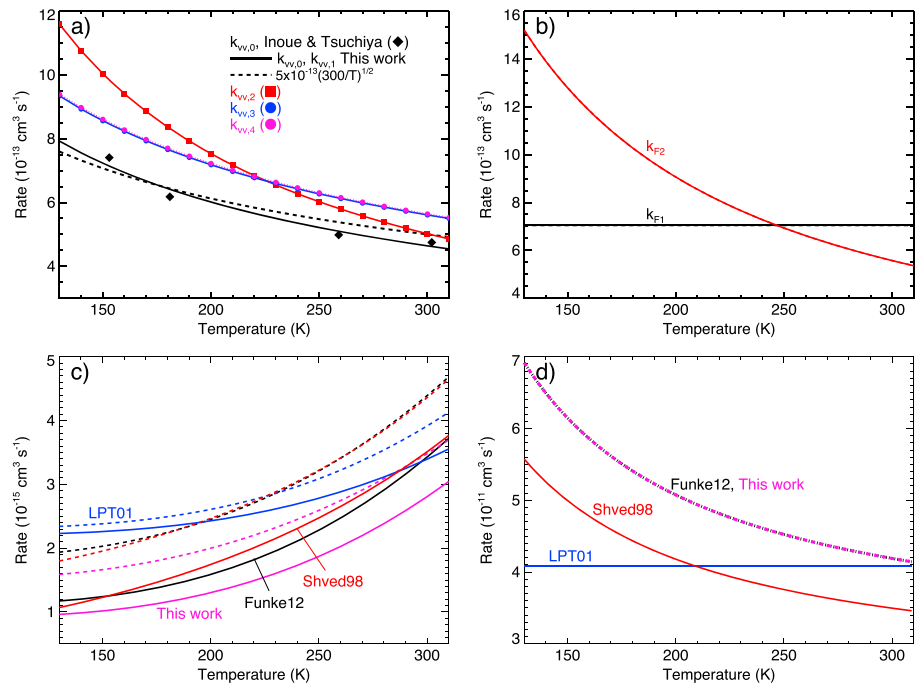


Figure 10. Temperature dependence of the collisional rates studied in this work. (a) $k_{vv,0}$ – $k_{vv,4}$. (b) k_{F1} and k_{F2} . (c) k_{vvi} ; the solid lines represents collisions with N_2 and dashed lines collisions with O_2 . (d) Excitation of $N_2(1)$ from $O(^1D)$. Labels indicate references as follows “Shved 98”: Shved *et al.* [1998], “LPT01”: López-Puertas and Taylor [2001], and “Funke12” Funke *et al.* [2012] (see text for more details).

The rate coefficient $k_{vv,2}$ is crucial for calculating the atmospheric radiation near 4.3 μm at upper mesospheric and lower thermospheric limb paths since the emission from the populations of the 10011 and 10012 levels, generating the second hot bands, are largely controlled by this rate. As for $k_{vv,1}$, this rate has also been taken equal to that of the fundamental band, $k_{vv,0}$, in all previous studies, including the analysis of the SPIRE emission near 2.7 μm [Sharma and Wintersteiner, 1985], except for SAMS and ISAMS. López-Puertas *et al.* [1998a, 1998b] found, as for $k_{vv,0}$, that a value between 0.8 and 1.0 times that of Inoue and Tsuchiya [1975] fitted better SAMS and ISAMS measurements. Note that López-Puertas and Taylor [1989] derived a rate twice that value but a subsequent analysis showed a factor of 0.8–1 [López-Puertas *et al.*, 1998a, 1998b]. The value derived here is significantly larger at temperatures smaller than 300 K, ranging from a factor of 1 to 1.5 from 300 K to 130 K, which is caused by the stronger temperature dependence retrieved here (compare red and black dashed lines in Figure 10a). This dependence could not be accounted for by the likely variability of, or change in, any other atmospheric or collisional parameter. This is a major result that significantly affects the 4.3 μm atmospheric limb radiances at tangent heights below around 85–95 km, particularly at polar summer conditions.

The rates for the V-V collisional energy exchange between N_2 and the high-energy levels $CO_2(v_d, v_3 = 1)$ with $v_d = 2v_1 + v_2 = 3$ and 4, $k_{vv,3}$ and $k_{vv,4}$, have also been considered equal to $k_{vv,0}$ in most of previous analysis. Only Funke *et al.* [2012] considered these rates to be different from $k_{vv,0}$, but they have not been used in the analysis of previous measurements. Here we have retrieved a temperature dependence slightly stronger than $1/\sqrt{T}$, $\alpha = 0.6$, and the values at mesospheric temperatures are also larger than previous rates in about 20%. We have not found any significant difference between $k_{vv,3}$ and $k_{vv,4}$.

The rates k_{F1} and k_{F2} retrieved here are shown in Figure 10b. These rates were very uncertain and a large range of values has been used in previous studies. Sharma and Wintersteiner [1985] derived values of $3 \cdot 10^{-11}$ and $1.5 \cdot 10^{-13} \text{ cm}^3 \text{ s}^{-1}$ for k_{F1} and k_{F2} , respectively, from their analysis of the spectrally resolved SPIRE measurements near 2.7 μm . They distinguished between the rate for process $CO_2(02211) + M \rightleftharpoons CO_2(10011)(k_{F2})$ and $CO_2(10012) + M \rightleftharpoons CO_2(02211)(k_{F2'})$, the latter being a factor 2 larger than the former. They made a thorough analysis of the spectra and concluded that those figures could be considered as lower limits. SAMS and ISAMS measurements near 4.3 μm are less sensitive to these rates. López-Puertas and Taylor [1989] and López-Puertas *et al.* [1998a, 1998b] analyzed those observations including values of $2 \cdot 10^{-11}$ and $2.4 \cdot 10^{-12} \text{ cm}^3 \text{ s}^{-1}$. These

values were based on the measurements of *Jacobs et al.* [1975] of $2 \cdot 10^{-11} \text{ cm}^3 \text{ s}^{-1}$ for the redistribution between the 10001 and 10002 levels, and on the results of *Finzi and Moore* [1975] who found that the redistribution of the v_1 and v_2 quanta is independent of the vibrational excitation of the v_3 mode. The k_{F1} and k_{F2} rates used in the model of *Shved et al.* [1998], which was used in the retrieval of CO_2 from CRISTA [*Kaufmann et al.*, 2002] and from SABER measurements [*Rezac et al.*, 2015], are $1.5 \cdot 10^{-13} \text{ cm}^3 \text{ s}^{-1}$ for k_{F1} and k_{F2} , and $3.0 \cdot 10^{-13} \text{ cm}^3 \text{ s}^{-1}$ for k_{F2} . Note that these rates differ significantly from those used in the other studies. We have retrieved a value of $7.04 \times 10^{-13} \text{ cm}^3 \text{ s}^{-1}$ for k_{F1} , constant with temperature; and larger values for k_{F2} , $5.57 \times 10^{-13} (300/T)^{1.2} \text{ cm}^3 \text{ s}^{-1}$, with a significant temperature dependence. The value for k_{F1} is about 43 times smaller than the rate derived by *Sharma and Wintersteiner* [1985] and about 4.7 times larger than that used by *Shved et al.* [1998]. For k_{F2} , our rate is about a factor of 9 to 5 (4.5 to 2.5 for k_{F2}) larger than those used by *Sharma and Wintersteiner* [1985] and *Shved et al.* [1998] for temperatures of 150 and 250 K, respectively. However, it is a factor of 2 to 3.5 (4 to 7 for k_{F2}) smaller for the same temperature interval when compared to those used in the SAMS and ISAMS analysis [*López-Puertas and Taylor*, 1989; *López-Puertas et al.*, 1998b]. Hence, we should expect significant changes in the simulation of atmospheric radiation of the three $4.3 \mu\text{m}$ second hot bands when using the new retrieved rates.

The k_{vt} collisional rates used in previous works and those retrieved here are shown in Figure 10c. The values reviewed by *López-Puertas and Taylor* [2001] (label LPT01) were used in the analysis of the SPIRE, SAMS, CLAES and ISAMS measurements [*Nebel et al.*, 1994; *López-Puertas and Taylor*, 1989; *Edwards et al.*, 1996; *López-Puertas et al.*, 1998a, 1998b]. *Shved et al.* [1998] used significantly smaller values, particularly at middle and low temperatures. *Funke et al.* [2012] revised the rates compiled in the review of *López-Puertas and Taylor* [2001] to lower values, which are very similar to those of *Shved et al.* [1998]. In this work we have retrieved values which are a factor of 0.82 smaller than those used by *Funke et al.* [2012].

The $k_{O(1D)}$ collisional rates and efficiencies used in previous works and those retrieved here are shown in Figure 10d. In the analysis of SPIRE [*Nebel et al.*, 1994], CLAES [*Edwards et al.*, 1996], and ISAMS data [*López-Puertas et al.*, 1998a, 1998b], the rate measured by *Amimoto et al.* [1979] of $2.4 \cdot 10^{-11} \text{ cm}^3 \text{ s}^{-1}$ was used with an efficiency in the transfer of electronic to vibrational energy of 25% (LPT01 in Figure 10d). *Shved et al.* [1998] used in their model a similar rate, which is larger at temperatures below $\sim 210\text{K}$ and smaller at larger temperatures (Figure 10d). More recently, *Funke et al.* [2012] has adopted the rate revised by *Ravishankara et al.* [2002] of $2.1 \cdot 10^{-11} \exp(115/T) \text{ cm}^3 \text{ s}^{-1}$ and assumed an efficiency of 20%. Here we have derived a value equal to that used by *Funke et al.* [2012] with an error of $\sim 15\%$.

To show the impact of the retrieved rates on the atmospheric limb spectral radiance near $4.3 \mu\text{m}$, we have performed simulations, for the April 45°N daytime (SZA = 44.5°) and the polar summer January 75°S (SZA = 58.7°) reference atmospheres, by utilizing a set of rate coefficients used in previous works and those retrieved here. As representative of previous works we have taken the rates of *Shved et al.* [1998]. Compared to other previous studies, these authors use similar values for $k_{vv,0}$, $k_{vv,1}$, $k_{vv,2}$, $k_{vv,3}$, and $k_{vv,4}$, and intermediate values for k_{F1} and k_{F2} . Further, they use a k_{vt} rate very similar to the more recent rate used by *Funke et al.* [2012], and an intermediate rate for $k_{O(1D)}$. All atmospheric parameters were considered the same in these simulations. Figure 11 shows the differences in the spectra at different tangent heights. Practically, all bands are affected at these tangent heights showing very large differences in the spectral shape. Compare, for example, the RMS (root-mean-square) values obtained for these two simulations with those obtained in the retrieval. They are factors of 8, 13, and 4 larger for tangent heights of 72, 81, and 90 km, respectively.

The radiance in the emission of the second hot bands SH1 and SH3 is about 20–30% smaller for the retrieved rates for tangent heights below around 90 km. This is a consequence of the larger retrieved $k_{vv,2}$ rate, leading to a significantly larger relaxation of the $2.7 \mu\text{m}$ levels. The emission of the SH2 band is, however, larger because of the larger retrieved k_{F2} rate, leading to a larger energy transfer from the states directly pumped by solar radiation (10011 and 10012) to 02211. As for the stronger SH1 and SH3 second hot bands, the emissions originating from the third and fourth hot bands are also smaller for the retrieved rates. This is also a consequence of the larger $k_{vv,3}$ and $k_{vv,4}$ rates retrieved here (compare $k_{vv,3}$ and $k_{vv,4}$ with the dashed line in Figure 10a).

The population of the 00011 level, responsible for the $4.3 \mu\text{m}$ emission of the fundamental band as well as the $10 \mu\text{m}$ band laser emissions, is very important for the atmospheric studies. In the lower-middle mesosphere its population is controlled, besides the solar pumping in the $4.3 \mu\text{m}$ band, by the V-V excitation through $\text{N}_2(1)$ from the $2.7 \mu\text{m}$ levels ($k_{vv,2}$ followed by $k_{vv,0}$), by the excitation of $\text{N}_2(1)$ from $\text{O}(1D)$ ($k_{O(1D)}$), and by the V-T

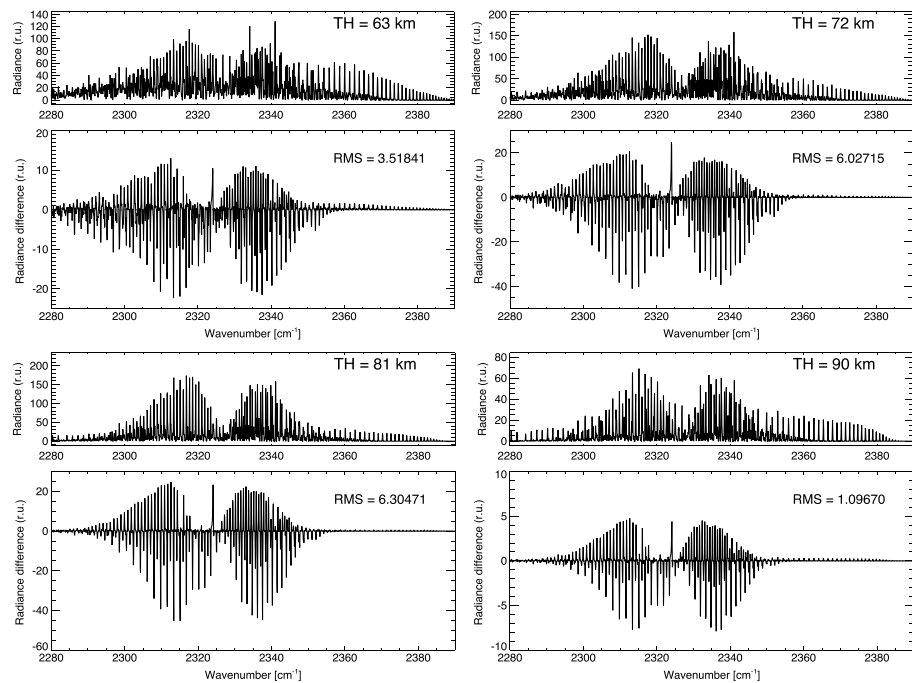


Figure 11. Simulation of MIPAS spectra for the retrieved rates and those mainly used in previous studies. Simulated spectra with the retrieved rates and differences (rates of this work – rates of previous works) at tangent heights of 63, 72, 81, and 90 km. Radiance units (r.u.) are in $nW/(cm^2 sr cm^{-1})$.

quenching with air molecules (k_{vt}). The $k_{v_{v,2}}$ rate derived here is significantly larger than those used in previous works, the excitation from $O(^1D)$ is similar, and the V-T thermal relaxation is moderately smaller. Overall, these processes lead to a larger excitation of 00011. In consequence the $4.3 \mu m$ fundamental band emission is larger for the new rates, in particular it is about 5% below around 90 km for midlatitude conditions.

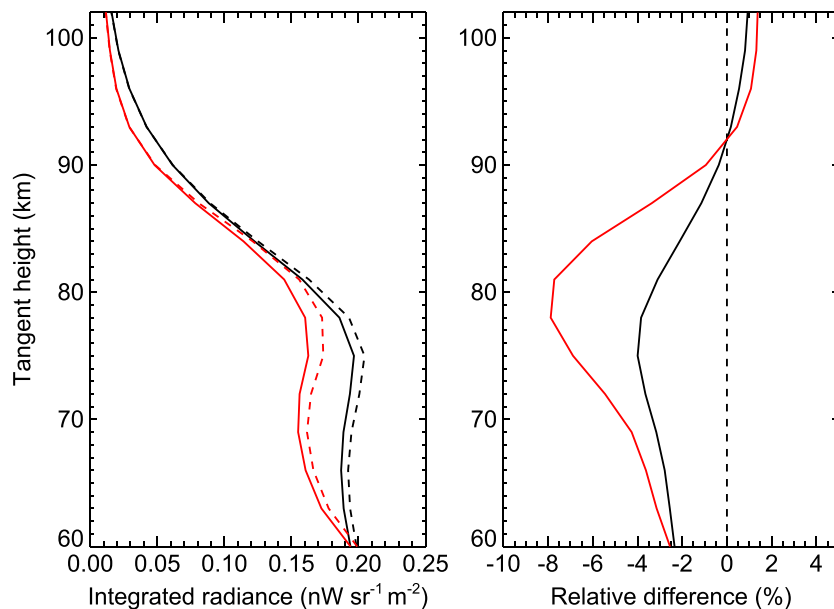


Figure 12. (left) Integrated limb radiance in the $2280-2400 cm^{-1}$ spectral range calculated for the April $45^{\circ}N$ ($SA = 44.5^{\circ}$) (in black) and for the polar summer January $75^{\circ}S$ ($SA = 58.7^{\circ}$) (in red) reference atmospheres [Funke et al., 2012] for a case of collisional rates used in previous works (see text) (dashed) and those retrieved here (solid). (right) The retrieved-previous work relative differences in percentage.

The overall effect for the integrated radiance in the 2280–2400 cm^{-1} spectral range is shown in Figure 12. The reduction in the second hot band dominates over the increase in the fundamental, resulting in a reduction in the radiance of 2–4% below about 85 km for midlatitude conditions and as much as 8% in the polar summer. At the uppermost tangent heights, where the emission from the fundamental band dominates, there is a small increase in about 1%.

9. Summary and Conclusions

We present here an analysis of the atmospheric limb spectra in the 4.3 μm region measured by MIPAS. This instrument has a high spectral resolution (0.0625 cm^{-1}) and a wide spectral coverage (from 685 to 2410 cm^{-1}) that allow measuring and discriminating among the many bands contributing to the atmospheric limb radiance near 4.3 μm . Further, MIPAS has a high sensitivity that allows measuring this atmospheric emission in a wide altitude range, from 20 to ~ 170 km. Hence, MIPAS spectra provide unique information on the non-LTE populations of the many CO_2 levels emitting in the 4.3 μm region and on the processes that control them. Our sensitivity study has shown that they contain significant information on the following collisional rates: (a) $k_{v_v,2}$, $k_{v_v,3}$, and $k_{v_v,4}$: $\text{CO}_2(v_d, v_3) + \text{N}_2 \rightleftharpoons \text{CO}_2(v_d, v_3 - 1) + \text{N}_2(1)$ with $v_d = 2v_1 + v_2 = 2$, $v_d = 3$, and $v_d = 4$, respectively; (b) k_{F1} and k_{F2} : $\text{CO}_2(v_1, v_2, l, 1, r) + \text{M} \rightleftharpoons \text{CO}_2(v'_1, v'_2, l', 1, r') + \text{M}$ with $\Delta v_d = 0$ and $\Delta l = 0$ (k_{F1}), and with $\Delta v_d = 0$, $\Delta l \neq 0$ (k_{F2}); (c) k_{v_t} , the thermal relaxation of $\text{CO}_2(v_3)$ to the v_1 and v_2 modes, e.g., $\text{CO}_2(v_d, v_3) + \text{M} \rightleftharpoons \text{CO}_2(v'_d, v_3 - 1) + \text{M}$ with $\Delta v_d = 2-4$ and $\Delta v_3 = -1$; and (d) on the efficiency of the excitation of $\text{N}_2(1)$ by $\text{O}(^1D)$.

A non-LTE retrieval scheme, used in previous analysis of the MIPAS non-LTE emission, has been applied to the MIPAS 4.3 μm spectra. The collisional rates described above, together with the CO_2 vmr have been retrieved from four days of MIPAS measurements (17 January, 30 March, 8 June, and 26 September of 2010) taken in its “Upper Atmosphere” mode (ranging from 40 to 170 km), covering solstice and equinox conditions and pole-to-pole latitudes. The wide altitude and latitude ranges have allowed to retrieve also the temperature dependence of the rates in the range of 130 to 250 K. The values obtained together with their temperature dependence and errors are shown in Table 1. All of them were retrieved with a much better accuracy that known before. The most salient results are as follows:

1. The $k_{v_v,2}$ derived here has a stronger temperature dependence than that used before. Also, it is significantly larger than previous values at temperatures below 300 K, ranging from a factor of 1 to 1.5 from 300 K to 130 K. This is a result of major importance since this rate controls the populations of the CO_2 (10011) and (10012) levels, and therefore, the atmospheric radiation near 4.3 μm and 2.7 μm at upper mesospheric and lower thermospheric limb paths.
2. The collisional rates for the V-V transfer from high-energy levels, $k_{v_v,3}$ and $k_{v_v,4}$, have been retrieved here for the first time. We have retrieved a temperature dependence of $1/T^{0.6}$, slightly stronger than $1/\sqrt{T}$, with values larger than previous rates by about 20% at mesospheric temperatures. We have not found any significant difference between $k_{v_v,3}$ and $k_{v_v,4}$.
3. We have retrieved values for the k_{F1} and k_{F2} rates very different from those previously used. k_{F1} is about 43 times smaller than the rate derived by *Sharma and Wintersteiner* [1985] and about 4.7 times larger than that used by *Shved et al.* [1998]. k_{F2} is about a factor of 9 to 5 (4.5 to 2.5 for $k_{F2'}$) larger than those used by *Sharma and Wintersteiner* [1985] and *Shved et al.* [1998] for temperatures of 150 and 250 K, respectively, and a factor of 2 to 3.5 (4 to 7 for $k_{F2'}$) smaller for the same temperature interval than those included in *López-Puertas and Taylor* [1989] and *López-Puertas et al.* [1998b]. This leads to significant changes in the modeled atmospheric radiation of the two stronger 4.3 μm second hot bands, decreasing them by 20–30% for midlatitude conditions.
4. The derived k_{v_t} collisional rate is slightly smaller (factor of 0.82) than the values used recently by *Funke et al.* [2012]. However, it is smaller by factors of 0.45 and 0.67 at 150 and 250 K than those used in the analysis of SPIRE, SAMS, and ISAMS measurements; and by factors of 0.83 and 0.76 than those used by *Shved et al.* [1998] and incorporated in the analysis of CRISTA and SABER measurements. The $k_{\text{O}(^1D)}$ collisional rate derived here jointly with k_{v_t} is very similar to that used by *Funke et al.* [2012]. This means that it is factors of 1.5 and 1.1 (at 150 and 250 K, respectively) larger than those used in the analysis of SPIRE, SAMS, and ISAMS measurements; and a factor of 1.21 larger than those used by *Shved et al.* [1998] and incorporated in the analysis of CRISTA and SABER measurements.

The new rates have very important effects on the atmospheric limb spectral radiances in the 10, 4.3, and 2.7 μm spectral regions when compared to typical collisional rates used in previous works. They lead to a reduction of the integrated radiance in the 2280–2400 cm^{-1} range of 2–4% at tangent heights below ~ 85 km for midaltitudes conditions, and as large as 8% for polar summer. This reduction is expected to be even larger in the 2.7 μm region. Also, a significant increase is expected in the 10 μm laser bands. Thus, these new rates allows a more accurate inversion of the CO_2 vmr in the mesosphere and lower thermosphere from measurements taken in the 10, 4.3, and 2.7 μm regions.

In a future work, we plan to retrieve the CO_2 vmr from the MIPAS spectra at 4.3 μm measured from 2005 until April 2012 by using the collisional rate coefficients derived here.

Acknowledgments

The IAA team was supported by the Spanish MCINN under grant AYA2011-23552 and the EC FEDER funds. The authors acknowledge ESA for providing MIPAS L1b spectra. These data can be obtained from the European Space Agency at <http://earth.esa.int/>. IMK/IAA-generated MIPAS data used in this study are available for registered users at <http://www.imk-asf.kit.edu/english/308.php>. ACE data can be obtained from https://database.scisat.ca/level2/ace_v3.5/ upon request. HITRAN data are publicly available from <https://www.cfa.harvard.edu/hitran/>.

References

- Amimoto, S. T., A. P. Force, J. R. G. Gulotty, and J. R. Wiesenfeld (1979), Collisional deactivation of $\text{O}(2^1D_2)$ by the atmospheric gases, *J. Chem. Phys.*, *71*, 3640.
- Beagley, S. R., C. D. Boone, V. I. Fomichev, J. J. Jin, K. Semeniuk, J. C. McConnell, and P. F. Bernath (2010), First multi-year occultation observations of CO_2 in the MLT by ACE satellite: Observations and analysis using the extended CMAM, *Atmos. Chem. Phys.*, *10*, 1133–1153.
- Brasseur, G., and S. Solomon (2005), *Aeronomy of the Middle Atmosphere—Chemistry and Physics of the Stratosphere and Mesosphere*, third ed., Atmospheric and Oceanographic Sciences Library 32, Springer, P. O. Box 17, 3300 AA, Dordrecht, Neth.
- De Laurentis, M., (2005), Planning of MIPAS new special modes January 2005 campaign, *Tech. Rep., ESA Technical Note, ENVI-SPPA-EOPG-TN-05-0002*, Eur. Space Agency, ESA-ESRIN, Frascati, Italy.
- Drummond, J. R., J. T. Houghton, G. D. Peskett, C. D. Rodgers, M. J. Wale, J. Whitney, and E. J. Williamson (1980), The stratospheric and mesospheric sounder on Nimbus 7, *Philos. Trans. R. Soc. London, Ser. A*, *296*, 219–241.
- Edwards, D. P., J. B. Kumer, M. López-Puertas, M. G. Mlynarczyk, A. Gopalan, J. C. Gille, and A. Roche (1996), Non-local thermodynamic equilibrium limb radiance near 10 μm as measured by CLAES, *J. Geophys. Res.*, *101*, 26,577–26,588.
- Ermolli, I., et al. (2013), Recent variability of the solar spectral irradiance and its impact on climate modelling, *Atmos. Chem. Phys.*, *13*(8), 3945–3977.
- Finzi, J., and C. B. Moore (1975), Relaxation of $\text{CO}_2(1001)$, $\text{CO}_2(0201)$, and $\text{N}_2\text{O}(1001)$ vibrational levels by near-resonant V-V energy transfer, *J. Chem. Phys.*, *63*(6), 2285–2288.
- Fischer, H., et al. (2008), MIPAS: An instrument for atmospheric and climate research, *Atmos. Chem. Phys.*, *8*, 2151–2188.
- Funke, B., M. López-Puertas, G. P. Stiller, T. von Clarmann, and M. Höpfner (2001), A new non-LTE retrieval method for atmospheric parameters from MIPAS-ENVISAT emission spectra, *Adv. Space Res.*, *27*(6–7), 1099–1104, doi:10.1016/S0273-1177(01)00169-7.
- Funke, B., M. López-Puertas, M. García-Comas, G. P. Stiller, T. von Clarmann, M. Höpfner, M. Glatthof, U. Grabowski, S. Kellmann, and A. Linden (2009), Carbon monoxide distributions from the upper troposphere to the mesosphere inferred from 4.7 μm non-local thermal equilibrium emissions measured by MIPAS on Envisat, *Atmos. Chem. Phys.*, *9*(7), 2387–2411.
- Funke, B., M. López-Puertas, M. García-Comas, M. Kaufmann, M. Höpfner, and G. P. Stiller (2012), GRANADA: A Generic RAdiative traNsfer AnD non-LTE population Algorithm, *J. Quant. Spectrosc. Radiat. Transfer*, *113*(14), 1771–1817, doi:10.1016/j.jqsrt.2012.05.001.
- García, R. R., M. López-Puertas, B. Funke, D. R. Marsh, D. E. Kinnison, A. K. Smith, and F. González-Galindo (2014), On the distribution of CO_2 and CO in the mesosphere and lower thermosphere, *J. Geophys. Res.*, *119*(9), 5700–5718, doi:10.1002/2013JD021208.
- García-Comas, M., et al. (2012), On the quality of MIPAS kinetic temperature in the middle atmosphere, *Atmos. Chem. Phys.*, *12*, 6009–6039, doi:10.5194/acp-12-6009-2012.
- García-Comas, M., et al. (2014), MIPAS temperature from the stratosphere to the lower thermosphere: Comparison of vM21 with ACE-FTS, MLS, OSIRIS, SABER, SOFIE and lidar measurements, *Atmos. Meas. Tech.*, *7*(11), 3633–3651.
- Gil-López, S., et al. (2005), Retrieval of stratospheric and mesospheric O_3 from high resolution MIPAS spectra at 15 and 10 μm , *Adv. Space Res.*, *36*(5), 943–951, doi:10.1016/j.asr.2005.05.123.
- Hase, F., P. Demoulin, A. J. Sauval, G. C. Toon, P. F. Bernath, A. Goldman, J. W. Hannigan, and C. P. Rinsland (2006), An empirical line-by-line model for the infrared solar transmittance spectrum from 700 to 5000 cm^{-1} , *J. Quant. Spectrosc. Radiat. Transfer*, *102*(3), 450–463, doi:10.1016/j.jqsrt.2006.02.026.
- Inoue, G., and S. Tsuchiya (1975), Vibration-vibration energy transfer of $\text{CO}_2(00^0_1)$ with N_2 and CO at low temperatures, *J. Phys. Soc. Jpn.*, *39*, 479–486.
- Jacobs, R. R., K. J. Pettipiece, and S. J. Thomas (1975), Rate constants for the CO_2 $02^0_0-10^0_0$ relaxation, *Phys. Rev. A*, *11*(1), 54–59.
- Kaufmann, M., O. A. Gusev, K. U. Grossmann, R. G. Roble, M. E. Hagan, C. Hartsough, and A. A. Kutepov (2002), The vertical and horizontal distribution of CO_2 densities in the upper mesosphere and lower thermosphere as measured by CRISTA, *J. Geophys. Res.*, *107*(D23), 8182, doi:10.1029/2001JD000704.
- Kaufmann, M., et al. (2006), Vibrationally excited ozone in the middle atmosphere, *J. Atmos. Sol. Terr. Phys.*, *68*(2), 202–212, doi:10.1016/j.jastp.2005.10.006.
- Kaufmann, M., Y. Zhu, M. Ern, and M. Riese (2014), Global distribution of atomic oxygen in the mesopause region as derived from SCIAMACHY O(1S) green line measurements, *Geophys. Res. Lett.*, *41*, 6274–6280, doi:10.1002/2014GL060574.
- Kiefer, M., T. von Clarmann, U. Grabowski, M. De Laurentis, R. Mantovani, M. Milz, and M. Ridolfi (2007), Characterization of MIPAS elevation pointing, *Atmos. Chem. Phys.*, *7*, 1615–1628, doi:10.5194/acp-7-1615-2007.
- Kurucz, R. L. (1995), The Kurucz Smithsonian atomic and molecular database, in *Astrophysical Applications of Powerful New Databases*, edited by S. J. Adelman and W. L. Wiese, p. 205, Astron. Soc. of the Pacific, San Francisco, Calif.
- Levenberg, K. (1944), A method for the solution of certain non-linear problems in least squares, *Quart. Appl. Math.*, *2*, 164–168.
- López-Puertas, M., and F. W. Taylor (1989), Carbon dioxide 4.3- μm emission in the Earth's atmosphere: A comparison between Nimbus 7 SAMS measurements and non-local thermodynamic equilibrium radiative transfer calculations, *J. Geophys. Res.*, *94*(D10), 13,045–13,068.
- López-Puertas, M., and F. W. Taylor (2001), *Non-LTE Radiative Transfer in the Atmosphere*, World Scientific Pub., Singapore.
- López-Puertas, M., G. Zaragoza, M. Á. López-Valverde, and F. W. Taylor (1998a), Non local thermodynamic equilibrium (LTE) atmospheric limb emission at 4.6 μm 1. An update of the CO_2 non-LTE radiative transfer model, *J. Geophys. Res.*, *103*(D7), 8499–8513.

- López-Puertas, M., G. Zaragoza, M. Á. López-Valverde, and F. W. Taylor (1998b), Non local thermodynamic equilibrium (LTE) atmospheric limb emission at 4.6 μm . An analysis of the daytime wideband radiances as measured by UARS improved stratospheric and mesospheric sounder, *J. Geophys. Res.*, *103*(D7), 8515–8530.
- López-Puertas, M., M. Á. López-Valverde, R. R. Garcia, and R. G. Roble (2000), A review of CO₂ and CO abundances in the middle atmosphere, in *Atmospheric Science Across the Stratopause*, *Geophys. Monogr. Ser.*, vol. 123, edited by M. López-Puertas et al., pp. 83–100, AGU, Washington, D. C.
- López-Puertas, M., et al. (2005), Atmospheric non-local thermodynamic equilibrium emissions as observed by the Michelson Interferometer for Passive Atmospheric Sounding (MIPAS), *C. R. Phys.*, *6*(8), 848–863, doi:10.1016/j.cry.2005.07.012.
- Marquardt, D. W. (1963), An algorithm for least-squares estimation of nonlinear parameters, *J. Soc. Indust. Appl. Math.*, *11*(2), 431–441.
- Mertens, C. J., et al. (2009), Kinetic temperature and carbon dioxide from broadband infrared limb emission measurements taken from the TIMED/SABER instrument, *Adv. Space Res.*, *43*(1), 15–27, doi:10.1016/j.asr.2008.04.017.
- Nebel, H., P. P. Wintersteiner, R. H. Picard, J. R. Winick, and R. D. Sharma (1994), CO₂ non-local thermodynamic equilibrium radiative excitation and infrared dayglow at 4.3 μm : Application to spectral infrared rocket experiment data, *J. Geophys. Res.*, *99*(D5), 10,409–10,419.
- Oelhaf, H., (2008), Mipasa mission plan, *ESA Tech. Note ENVI-SPPA-EOPG-TN-07-0073*, Eur. Space Agency, ESA-ESRIN, Frascati, Italy.
- Perron, G., G. Aubertin, R. Desbiens, T. Fehr, F. Niro, A. Kleinert, M. Kiefer, M. Birk, and G. Wagner (2010), Mipasa level 1b algorithm evolutions, in *ESA Living Planet Symposium*, vol. SP-686, pp. 33–36, ESTEC, Noordwijk, Netherlands.
- Picone, J., A. Hedin, D. Drob, and A. Aikin (2002), NRLMSISE-00 empirical model of the atmosphere: Statistical comparisons and scientific issues, *J. Geophys. Res.*, *107*(A12), 1468, doi:10.1029/2002JA009430.
- Platnick, S., and J. M. Fontenla (2008), Model calculations of solar spectral irradiance in the 3.7- μm band for Earth remote sensing applications, *J. Appl. Meteorol. Climatol.*, *47*(1), 124–134.
- Raspollini, P., et al. (2010), Level 2 near-real-time analysis of MIPAS measurements on ENVISAT, in *Eight Years of MIPAS Measurements*, vol. SP-686, pp. 011–d2, ESTEC, Noordwijk, Netherlands.
- Ravishankara, A., E. Dunlea, M. Blitz, T. Dillon, D. Heard, M. Pilling, R. Strekowski, J. Nicovich, and P. Wine (2002), Redetermination of the rate coefficient for the reaction of O(¹D) with N₂, *Geophys. Res. Lett.*, *29*(15), 1745, doi:10.1029/2002GL014850.
- Rezac, L., A. Kutepov, J. M. III. Russell, A. G. Feofilov, J. Yue, and R. A. Goldberg (2015), Simultaneous retrieval of T(p) and CO₂ VMR from two-channel non-LTE limb radiances and application to daytime SABER/TIMED measurements, *J. Atmos. Sol. Terr. Phys.*, *130–131*, 23–42, doi:10.1016/j.jastp.2015.05.004.
- Rienecker, M. M., et al. (2011), MERRA: NASA's Modern-Era Retrospective Analysis for Research and Applications, *J. Clim.*, *24*(14), 3624–3648, doi:10.1175/jcli-d-11-00015.1.
- Rinsland, C. P., and A. Goldman (1992), Search for infrared absorption lines of atmospheric chlorine monoxide (ClO), *J. Quant. Spectrosc. Radiat. Transfer*, *48*(5/6), 685–692.
- Rodgers, C. D. (2000), *Inverse Methods for Atmospheric Sounding: Theory and Practice*, *Series on Atmospheric, Oceanic and Planetary Physics*, vol. 2, edited by F. W. Taylor, World Scientific Publishing Co. Pte. Ltd, Singapore.
- Rothman, L. S., and L. D. G. Young (1981), Infrared energy levels and intensities of carbon dioxide—II, *J. Quant. Spectrosc. Radiat. Transfer*, *25*, 505–524, doi:10.1016/0022-4073(81)90026-1.
- Rothman, L. S., et al. (2005), The HITRAN 2004 molecular spectroscopic database, *J. Quant. Spectrosc. Radiat. Transfer*, *96*, 139–204, doi:10.1016/j.jqsrt.2004.10.008.
- Rothman, L. S., et al. (2009), The HITRAN 2008 molecular spectroscopic database, *J. Quant. Spectrosc. Radiat. Transfer*, *110*, 533–572, doi:10.1016/j.jqsrt.2009.02.013.
- Sharma, R. D., and P. P. Wintersteiner (1985), CO₂ component of daytime Earth limb emission at 2.7 micrometers, *J. Geophys. Res.*, *90*(A10), 9789–9803.
- Shved, G. M., A. A. Kutepov, and V. P. Ogibalov (1998), Non-local thermodynamic equilibrium in CO₂ in the middle atmosphere. I. Input data and populations of the ν_3 mode manifold states, *J. Atmos. Sol. Terr. Phys.*, *60*(3), 289–314.
- Stiller, G. P., T. von Clarmann, B. Funke, N. Glatthor, F. Hase, M. Höpfner, and A. Linden (2002), Sensitivity of trace gas abundances retrievals from infrared limb emission spectra to simplifying approximations in radiative transfer modelling, *J. Quant. Spectrosc. Radiat. Transfer*, *72*(3), 249–280, doi:10.1016/S0022-4073(01)00123-6.
- Tikhonov, A. (1963), On the solution of incorrectly stated problems and method of regularization, *Dokl. Akad. Nauk. SSSR*, *151*(3), 501–504.
- von Clarmann, T., and G. Echle (1998), Selection of optimized microwindows for atmospheric spectroscopy, *Appl. Opt.*, *37*(33), 7661–7669.
- von Clarmann, T., et al. (2003a), Remote sensing of the middle atmosphere with MIPAS, in *Remote Sensing of Clouds and the Atmosphere VII*, vol. 4882, edited by K. Schäfer et al., pp. 172–183, SPIE, Bellingham, Wash.
- von Clarmann, T., et al. (2003b), Retrieval of temperature and tangent altitude pointing from limb emission spectra recorded from space by the Michelson Interferometer for Passive Atmospheric Sounding (MIPAS), *J. Geophys. Res.*, *108*(D23), 4736, doi:10.1029/2003JD003602.